Paleoceanography and Paleoclimatology

RESEARCH ARTICLE
10.1029/2020PA004058

A Multi-Proxy Approach to Unravel Late Pleistocene Sediment Flux and Bottom Water Conditions in the Western South Atlantic Ocean

G. L. Mathias[1,2,3], S. C. Roud[4], C. M. Chiessi[1], M. C. Campos[1], B. B. Dias[5], T. P. Santos[5], A. L. S. Albuquerque[5], F. A. L. Toledo[6], K. B. Costa[6], and B. A. Maher[2]

[1]School of Arts, Sciences and Humanities, University of São Paulo, São Paulo, Brazil, [2]Lancaster Environment Centre, University of Lancaster, Lancaster, UK, [3]Institute of Geosciences, University of São Paulo, São Paulo, Brazil, [4]Department of Earth and Environmental Sciences, Ludwig-Maximilians University of Munich, Munich, Germany, [5]Geochemistry Graduate Program, Fluminense Federal University, Niterói, Brazil, [6]Oceanographic Institute, University of São Paulo, São Paulo, Brazil

Key Points:

- Multi-proxy approach points to the Plata River as the main lithogenic sediment source to tropical SE South American continental margin, modulated by sea-level
- Reduced biogenic magnetite formation coeval with negative benthic $\delta^{13}C$ anomalies during glaciations
- Biogenic magnetite formation hampered by decreased bottom water ventilation during glaciations

Supporting Information:

- Supporting Information S1

Correspondence to:
G. L. Mathias,
g.mathias@alumni.usp.br

Citation:
Mathias, G. L., Roud, S. C., Chiessi, C. M., Campos, M. C., Dias, B. B., Santos, T. P., et al. (2021). A multi-proxy approach to unravel late Pleistocene sediment flux and bottom water conditions in the western South Atlantic Ocean. *Paleoceanography and Paleoclimatology*, *36*, e2020PA004058. https://doi.org/10.1029/2020PA004058

Received 27 JUL 2020
Accepted 4 FEB 2021

Abstract Magnetic signals in deep-sea sediments have the potential to unravel past continental environmental changes, via changes in primary terrigenous magnetic supply, but also record past marine environmental conditions, via in situ formation of secondary magnetic minerals, particularly when complemented by independent proxies. By combining environmagnetic, geochemical, and siliciclastic grain size data, we investigated marine sediment core GL-1090 (24.92°S, 42.51°W, 2,225 m water depth) aiming to unravel changes in terrigenous sediment input and bottom water conditions during the last ~184 ka at the western South Atlantic middepth. The Al/Si, Fe/κ and siliciclastic grain size data show that terrigenous sediments at this core location derived from the Plata River (southeastern South America). This material was transported northwards by the Brazilian Coastal Current and their delivery to our core site was modulated by sea-level oscillations. Periods of low sea-level were characterized by the input of coarser and more abundant terrigenous sediments. Environmagnetic parameters indicate significant downcore variations in the magnetic domain state, which we interpret as changes in the content of biogenic magnetite following glacial-interglacial cycles. Coeval negative excursions in magnetic grain size and benthic $\delta^{13}C$ suggests that concentrations of single domain magnetite (possibly magnetotactic bacterial magnetite) vary in response to middepth water ventilation. We suggest that reduced ventilation in the middepth western South Atlantic bottom waters during peak glaciations triggered a decrease in the production of biogenic magnetite. Peak glaciations were, in turn, linked with increases in the residence time of North Atlantic Deep Water (or its glacial counterpart).

1. Introduction

Combining rock-magnetic proxies with bulk sediment characteristics has been proven useful to unravel the composition of the primary minerals present in the sediment, transport dynamics in different marine settings and sediment provenance (Hounslow & Maher, 1999; Itambi et al., 2009; Just, Dekkers, et al., 2012; Mathias et al., 2014; Razik et al., 2013). In turn, marine sediments are widely used to reconstruct continental paleoclimate, often based on major element composition. Relative changes in major element concentrations provide insights into weathering intensity in the source area (Sheldon & Tabor, 2009), paleoenvironments in the continent (Just, Heslop, et al., 2012), and sediment transport pathways (Mulitza et al., 2008; Portilho-Ramos et al., 2017). Changes in marine sediment may also be recorded in the magnetic as well as bulk mineral assemblies. Care is always needed as sedimentary minerals may have been formed in the source area (primary assembly) and/or after deposition, during early diagenesis (authigenic assembly) (Chang, Bolton, et al., 2016; Funk et al., 2004). In terms of authigenesis, the presence of bacterial magnetosome particles can often be inferred within the sedimentary "haystack" due to some characteristic magnetic "fingerprints", even if they constitute only a minor fraction of the bulk magnetic assemblage (Egli et al., 2010; Roberts et al., 2012). If preserved, this additional biogenic magnetic component may provide unique insights into past benthic microbial activity and bottom water conditions effective when the sediments were deposited.

Transported terrigenous magnetic minerals form the primary magnetic assemblage of marine sediments. Their concentration, composition and size distribution are a function of the geologic characteristics of the source area, weathering conditions and transport mechanisms, each potentially leaving characteristic fingerprints on the marine sedimentary magnetic assemblage (Evans & Heller, 2003; Liu et al., 2012; Maher & Thompson, 1999; Thompson & Oldfield, 1986; Verosub & Roberts, 1995). The western South Atlantic is bathed by diverse water masses from remote areas (i.e., Southern Ocean, northern North Atlantic Ocean, and Indian Ocean) and receives terrigenous sediments from multiple drainage basins in South America. In subtropical latitudes, one large (i.e., Plata River) and many small (e.g., Paraíba do Sul River) drainage basins occupy southeastern South America and deliver terrigenous sediments to the western South Atlantic (Razik et al., 2015). Changes in sediment production, transport and delivery over southeastern South America are expected to affect the terrigenous infill of the subtropical western South Atlantic. In mid-depths (~2,000 m), the western South Atlantic is influenced by the southward-flowing Deep Western Boundary Current that transports North Atlantic Deep Water (NADW) (Stramma & England, 1999). During deposition, the terrigenous material can be "diluted" by primary production of carbonate and opal, while the magnetic assemblage can be altered through the production of biogenic magnetic minerals by benthic microorganisms. Additionally, during early diagenesis, all magnetic minerals may undergo chemical alterations (oxidation, reduction, dissolution) depending on the redox conditions of the sediment (Chang, Roberts, et al., 2014; Hounslow & Maher, 1999; Karlin et al., 1987; Lovley et al., 1987; Roberts, Florindo, et al., 2011). Under sulphidic conditions, additional magnetic information can arise through the formation of magnetic sulphide minerals (Roberts, Chang, et al., 2011). Because the complete history of sediments, from source to sink including diagenetic alteration, can leave characteristic marks on the magnetic mineral assemblage, sedimentary magnetic properties comprise a powerful, if sometimes complex, tool to disentangle the driving forces of sediment supply and transformation. Biogenic magnetic particles produced by magnetotactic bacteria (MTB) appear almost ubiquitous in surface sediments (Maher & Hounslow, 1999; Roberts et al., 2012). Such bacteria commonly live near the sediment-water interface in the chemically stratified horizons spanning the oxic to anoxic transition (e.g., Faivre & Schüler, 2008). MTB biomineralize intracellular, membrane-bound magnetic nanoparticles, called magnetosomes, which are composed of magnetite (Fe_3O_4) or greigite (Fe_3S_4) depending on the redox conditions of their habitat (Bazylinski et al., 1995; Chen et al., 2014). The ecological roles of these particles remain unresolved but they are often ideal single-domain (SD) magnets that passively align the microorganisms with the Earth's magnetic field, suggesting some contribution to directed motility. The long intracellular chains of dense magnetite may also provide some cellular structural support (Hanzlik et al., 1996). If preserved in the sedimentary record, the MTB magnetofossils register past microbial activity and sediment chemistry. Their abundance has been linked to paleo-environmental and sedimentary conditions (Hesse, 1994; Kopp & Kirschvink, 2008; Maher & Hounslow, 1999; Roberts, Florindo, et al., 2011). Although it has been demonstrated that the number of living MTB undergoes seasonal changes (Du et al., 2015; He et al., 2018) and that magnetofossil abundance in deep-sea sediments can be modulated by organic carbon and dissolved iron availability (Roberts, Florindo, et al., 2011) or by primary productivity (Savian et al., 2014), our understanding of the conditions responsible for MTB magnetic mineral formation is still limited.

Here we provide new magnetic, geochemical, and siliciclastic grain size data from a core collected from the middepth western South Atlantic (24.92°S, 42.51°W, 2,225 m water depth) covering the last 184 ka. Changes in the concentration of magnetic minerals, major elements, and siliciclastic grain size suggest Plata River as the main source of the terrigenous material deposited in the subtropical western South Atlantic, with a mixing of terrigenous material from Paraíba do Sul River modulated by sea-level oscillations. In addition, we observed relationships among variations in magnetic grain size, benthic foraminifera $\delta^{13}C$ (Santos et al., 2017), and total organic carbon (Figueiredo et al., 2020), which suggest a potential connection between bottom water ventilation and single domain, possibly bacterial magnetite abundance. Magnetic grain size changes in response to glacial and interglacial stages may offer new insights into the influence of NADW (or its glacial counterpart) ventilation on bacterial magnetite abundance.

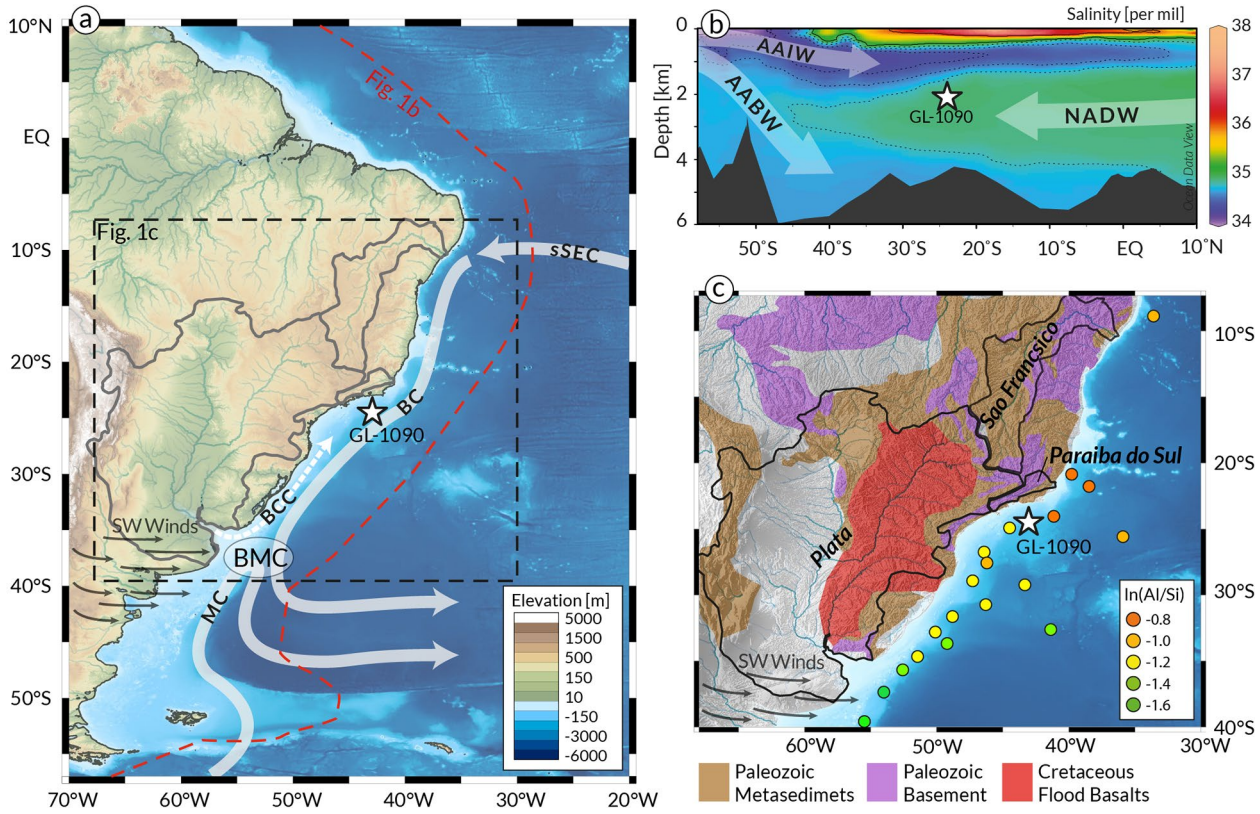

Figure 1. Overview of the study area. The location of marine sediment core GL-1090 is shown in each panel by a white star. (a) Topographic map of South America with the catchment area of rivers of interest that drain into the western South Atlantic outlined in black. The white arrows over the bathymetric map of the South Atlantic schematically depict the surface currents of interest (i.e., Brazilian Coastal Current [BCC], Brazil Current [BC] and Malvinas Current [MC]) as well as the Brazil-Malvinas Confluence (BMC). Thinner gray arrows show the Westerlies. The red and black dashed lines indicate the position of the salinity transect in Figure 1b and the location of Figure 1c, respectively. Topography and bathymetry from ETOPO1 (Amante & Eakins, 2009). (b) Western South Atlantic modern mean annual salinity (color shading; Zweng et al., 2013). Main water masses are depicted by the gray arrows, Antarctic Intermediate Water (AAIW), North Atlantic Deep Water (NADW) and Antarctic Bottom Water (AABW). (c) Simplified geology of the major drainage basins, outlined in black, that represent relevant source areas for terrigenous material in the study area (geology simplified after/adapted from "World CGMW, 1:50M, Geologic Units Onshore" with sedimentary overburden removed) (Commission for the Geological Map of the World). Major tributaries of the Plata River are shown in blue. Colored dots on the adjacent continental margin indicate surface sediment ln(Al/Si) values after Govin et al. (2012). This figure was partially produced using the software Ocean Data View (Schlitzer, 2019).

2. Study Area

2.1. Hydrographic Setting, Sediment Redistribution

Figures 1a and 1b shows the complex oceanographic setting of the western South Atlantic. On the continental shelf (upper 100 m of the water column), Plata River discharge is transported to the north by the Brazilian Coastal Current (BCC) (Piola et al., 2005; Souza & Robinson, 2004). Satellite observations of sea surface salinity and temperature suggest that the modern BCC reaches as far north as 25°S (Souza & Robinson, 2004). Magnetic studies of Holocene sediments, however, suggest that the Plata River plume has delivered sediments further north, up to at least 24°S (Mathias et al., 2014).

Beyond the shelf break, the upper 500 m of the water column is dominated by the southward transport of the Brazil Current (BC) which originates from the southern branch of the South Equatorial Current at about 10°S. The BC transports the warm and saline equatorial waters poleward until it collides with the northward-flowing Malvinas Current and is deflected to the east (Peterson & Stramma, 1991; Stramma & England, 1999). This convergence area, the Brazil-Malvinas Confluence Zone, is located around 33–38°S offshore the Plata River mouth (Figure 1a).

From 500 m down to intermediate depths (~1,200–1,500 m water depth), the Intermediate Western Boundary Current (IWBC) transports Antarctic Intermediate Water (AAIW) and Upper Circumpolar Deep Water (UCDW) toward the north (Figure 1b) (Boebel et al., 1999). The southern-sourced AAIW and UCDW are relatively fresh, cold, nutrient-enriched and oxygen-depleted water masses (Tsuchiya et al., 1994). NADW fills the mid-depths of the water column between ~1,200 and 3,000 m water depth (Stramma & England, 1999). NADW, a nutrient-depleted and oxygen-enriched water mass, has a similar temperature but is saltier than its overlying water mass (Tsuchiya et al., 1994). NADW is transported southwards by the Deep Western Boundary Current, and at 25°S reaches maximum salinity (~0.35 psu) in its deepest part (Stramma & England, 1999).

2.2. Geological Setting, Sediment Sources

Southeastern South America is characterized by the presence of the Serra do Mar and Serra da Mantiqueira mountain ranges close to the Atlantic coastline that forces rivers to drain into the hinterland and deviate from this topographic barrier before reaching the western South Atlantic. The narrow coastal plain adjacent to our core location, dominated by Precambrian basement and Fe oxide-rich meta-sediments, is drained by a number of minor rivers with a combined drainage area of $\sim 6 \times 10^5$ km^2 (Figure 1c). Among these rivers, the Paraíba do Sul is closest to our study site (~20°S, 41°W), and drains a small catchment area (5.7×10^4 km^2) of which more than 90% is covered by Precambrian rocks, with predominance of granitoid gneisses, migmatites, biotite-gneiss and biotite schists (Gómes Tapias et al., 2019). The two major basins that drain the hinterland before reaching the western South Atlantic host the São Francisco and Plata rivers. The São Francisco River drains an area of $\sim 6 \times 10^5$ km^2 of Precambrian hinterland into the tropical Atlantic at ~ 10°S (ca. 15° north of our study site). About 10° south of our study site (~35°S, 57°W), the Plata River meets the subtropical Atlantic Ocean. Its tributaries, the Paraná and Uruguay rivers, drain an area five times bigger than the São Francisco Basin ($\sim 3.2 \times 10^6$ km^2). The Plata Basin represents the largest source of terrigenous material to the western South Atlantic and ranges from the Mesozoic-Tertiary Andean Mountains in the west to the Cretaceous Flood Basalts (Paraná-Etendeka igneous province) in the east (Gómes Tapias et al., 2019). With only minor riverine input in close proximity, the sedimentary dynamics at the core site is primarily controlled by sediment redistribution by ocean currents, and primary carbonate production; both modulated by climatic and sea-level changes (Mahiques et al., 2008; Razik et al., 2015).

In addition to riverine transport of detrital material to the continental margin of southeastern South America, the westerlies play an important role in transporting dust from the Andes to the mid-latitudes off southern South America (e.g., Gaiero et al., 2003). During dry glacial climate stages, enhanced generation and transport of aeolian dust increased the transport of terrigenous material to the Argentinean and Uruguayan continental shelves (e.g., Maher et al., 2010).

3. Materials and Methods

3.1. Core GL-1090

Marine sediment core GL-1090 is 1,914 cm long and was collected from the continental slope (2,225 m water depth) of southeastern South America (24.92°S, 42.51°W) (Figure 1), in a region bathed by the NADW. GL-1090 is mostly composed of carbonate mud. According to Santos et al. (2017), greenish to olive sediments somewhat rich in foraminifera-bearing silty clay characterize glacial layers. Carbonate-rich reddish-brown and whitish clays characterize interglacial sediments. At about 30 cm core depth, there is a ~ 2 cm-thick ferruginous crust.

3.2. Age Model

The age model for core GL-1090 was published in Santos et al. (2017) and is based on 10 accelerator mass spectrometer radiocarbon ages from planktonic foraminifera (covering the top 327 cm), combined with 13 benthic foraminifera $\delta^{18}O$ tie-points aligned to two reference curves (Govin et al., 2014; Lisiecki & Raymo, 2005) for the lower part of the core (327–1,914 cm). Core GL-1090 covers the last ~184 ka. The mean sedimentation rate for core GL-1090 is 13 cm/ka. Highest rates were observed during MIS 4 with 24 cm/ka.

During MIS 5e, MIS 5d and MIS 1 the sedimentation rates are smaller than 5 cm/ka, with minimum of 3 cm/ka. The complete age model and details on the methodology used to produce it can be found in Santos et al. (2017).

3.3. Rock Magnetism

For the rock magnetic characterization of the sediment core, a series of laboratory magnetization and demagnetization experiments were carried out on unorientated samples in plastic cylinders (16 cm^3 volume). We measured volume magnetic susceptibility (κ) on the whole core with a 2 cm resolution using a 130 mm diameter Bartington loop sensor (MS2C) integrated with a Geotek Multi-Sensor Core Logger system. For 101 of the single samples, we imparted an anhysteretic remanent magnetization (ARM) at 300 mT using a bias field of 0.1 mT. Thereafter, we demagnetized the ARM on these samples using 77 steps up to 300 mT, as suggested by Egli (2004). The ARM was acquired, measured and demagnetized using a 2G Enterprises RAPID magnetometer 755 (noise level 5×10^{-12} Am^2) housed in a magnetically shielded room (ambient field <500 nT) at the Laboratory of Paleomagnetism (USPMag), Institute of Astronomy, Geophysics and Atmospheric Sciences (IAG), University of São Paulo, Brazil. We imparted isothermal remanent magnetization (IRM) to 163 samples in three steps (at 100, 300, and 1,000 mT), and backfields at −100 and−300 mT using a magnetizer Newport 4″ Electromagnet Type A (0–1.5 Tesla) and measured the IRMs with a Molspin fluxgate spinner magnetometer (noise level $\sim 5 \times 10^{-10}$ Am^2) at the Center for Environmental Magnetism and Paleomagnetism (CEMP), University of Lancaster, United Kingdom.

From these measurements, we derived typical environmental magnetic proxies to determine type, size and concentration of the magnetic carriers (e.g., Evans & Heller, 2003; Maher & Thompson, 1999). The susceptibility (κ) measures the induced magnetization of the bulk sediment, and is often dominated by ferrimagnetic materials. Magnetic susceptibility of ferrimagnetic minerals (up to $\sim 57 \times 10^{-6}$ m^3kg^{-1} e.g., magnetite) is orders of magnitude larger than antiferromagnetic ($\sim 0.5 \times 10^{-6}$ m^3kg^{-1}, e.g., hematite), paramagnetic ($\sim 0.4 \times 10^{-6}$ m^3kg^{-1}, e.g., clay minerals) and diamagnetic (-0.005×10^{-6} m^3kg^{-1}, e.g., carbonate) materials (Maher, 1998). Paramagnets and diamagnets have minor contributions to bulk sediment susceptibility in comparison to ferrimagnetic minerals, yet dilution effects may affect the total susceptibility (Hounslow & Maher, 1999). The geochemical/magnetic proxy Fe/κ is a relative measure of how much of the total Fe is bound in magnetic minerals. The IRM is representative of the total concentration of magnetic minerals. Differences between the IRM acquired at 300 mT (IRM_{300}) and 1 T (SIRM) reveal contributions of different magnetic mineral types. The S-Ratio (=(IRM_{300}/SIRM)/2) can track relative mineralogical changes of magnetically "hard" versus "soft" minerals (Bloemendal et al., 1992). HIRM (=(SIRM + IRM_{-300})/2) is useful in quantifying relative concentrations of the high-coercivity (magnetically "hard") mineral, like hematite (Maher et al., 2004).

The ARM represents mainly the low-coercivity ferrimagnetic mineral fraction (usually magnetite) and is selective toward the stable single domain grains that exhibit ARMs 1–2 orders of magnitude greater than larger grains (Maher, 1988; Peters & Dekkers, 2003). Ratios of ARM/IRM are thus sensitive to relative changes in grain size. Here we use $\chi ARM_{300mT}/IRM_{100mT}$ (χARM/IRM hereafter) to detect changes in magnetite grain size. ARM_{300} was converted to susceptibility of ARM (χARM) by normalizing with the bias field (79.625 A/m).

We further characterized 72 representative sub-samples by measuring hysteresis loops, stepwise IRM acquisition and backfield curves with maximum fields of 1T. We used a Princeton Measurements Corporation MicroMag 3900 Vibrating Sample Magnetometer at both the Laboratory of Paleomagnetism (USPMag), Institute of Astronomy, Geophysics and Atmospheric Sciences (IAG), University of São Paulo, and at the Paleomagnetism and Environmental Magnetism Laboratory, National Oceanography Center (NOC), Southampton, United Kingdom.

From hysteresis loops and backfield curves, we obtained the saturation remanence (Mrs), saturation magnetization (Ms), the coercive field (Bc) and the coercivity of remanence (Bcr). The ratios Mrs/Ms and Bcr/Bc provide information on the magnetite grain size and resultant domain structures of the magnetic particles, indicative of different grain size thresholds: superparamagnetic (SP), single-domain (SD), pseudo-single domain (PSD), and multidomain (MD) (Dunlop & Özdemir, 1997). A cross plot of the two ratios allows

some preliminary assessment of the average domain state (i.e., magnetic grain size), identification of relative grain size changes and checking the presence of different types of magnetic minerals (Dunlop, 2002).

For a more detailed characterization of the finest magnetite fraction, we measured high-resolution first-order reversal curves (FORC) of seven subsamples representing horizons of different glacial stages. These measurements were performed in a Princeton Measurements Corporation vibrating sample magnetometer at the Department of Earth and Environmental Sciences, Ludwig-Maximilians, University of Munich, Germany. The measuring protocol was optimized to selectively cover the central ridge area of the FORC diagram that characterizes SD particle distribution. (H_b: −10/+20 mT, H_c: 0–80 mT, H_{Sat}: 300 mT, increment 0.5 mT (N:233), averaging time: 120 ms, sample mass: 0.2 g). The FORC distributions were calculated using VARIFORC (Egli, 2013) by averaging 10 high-resolution measurements per sample, applying variable smoothing and extracting the central ridge feature. Variable smoothing factor was applied to reduce noise in the low amplitude areas of the FORC space and increase the resolution of the central ridge (VARIFORC processing parameters: sc,0 = 4, sc,1 = sb,1 = 5, λc = λb = 0.1).

3.4. Major Elements

X-ray fluorescence (XRF) core scanner data were collected every 5 mm down-core over a 60 mm^2 area (down-core slit size of 5 mm using generator settings of 10 kV, a current of 0.35 mA, and a sampling time of 20 s), directly from the split core surface of u-channels collected from the archive half of core GL-1090. The data were collected using the XRF Core Scanner II (AVAATECH Serial No. 2) at the Center for Marine Environmental Sciences (MARUM), University of Bremen, Germany. The split-core surface was covered with a 4 μm thin SPEXCerti Prep Ultralene1 foil to avoid contamination of the XRF measurement unit and desiccation of the sediment. The element data reported here were acquired by a Canberra X-PIPS Silicon Drift Detector (SDD; Model SXD 15C-150-500) with 150 eV X-ray resolution, the Canberra Digital Spectrum Analyzer DAS 1000, and an Oxford Instruments 50W XTF5011 X-ray tube with rhodium (Rh) target material. Recently, Figueiredo et al. (2020) published XRF core scanner data from core GL-1090 in counts for the elements Ti, Al, Fe, Mn, and Ca. Here we present major element concentrations obtained from bulk sediment samples in order to cross-calibrate the scanner counts. We freeze-dried, powdered, and homogenized 55 samples (~5 g of dry sediment). Major element concentrations were measured by energy dispersive polarization X-ray fluorescence (EDP-XRF) spectroscopy at the Department of Geochemistry, Fluminense Federal University, Brazil. We performed the calibration using a log-ratio approach after Weltje and Tjallingii (2008). The log ratios of major element (Al, Si, K, Ca, Ti, Mn, S, and Fe) and Ca as denominator were calculated. The log-ratios of the core scanner data were then calibrated to the corresponding ratios of the powder measurements through linear regression. Figure S1 shows the comparison between EDP discrete data and calibrated curve with XRF counting.

We show elemental concentrations of Al, Si, K, Ti, and Fe considered to represent terrigenous contributions, and Ca, representing the biogenic calcium carbonate fraction of the bulk sediment (Govin et al., 2012). Assuming that terrigenous Fe and Ti have a common origin (Figure S2a), we used the immobile element Ti as a normalizer for Fe, aiming to assess if the iron distribution in the sediment has been altered after deposition. The terrigenous fraction of the bulk sediment can be further characterized by the elemental ratios, Al/Si, which reflects compositional and/or grain size changes in the siliciclastic mineral fraction, and Fe/K, which responds to changes in the clay mineral composition and reflects weathering intensity (Govin et al., 2012). Since Fe can be remobilized in the sediment after deposition (Reitz et al., 2004), in this study we used K/Ti to identify weathering intensity in the continent, as K derives from minerals characteristic from dry regions, like potassium feldspar and illite (Zabel et al., 2001).

3.5. Siliciclastic Grain Size

Particle size measurements of sediment core GL-1090 were performed in a particle analyzer via laser diffraction (CILAS 1064) in the Department of Geochemistry at Fluminense Federal University, Brazil. The analysis was performed on decalcified and organic matter-free samples, by the addition of HCl 1M and 30% hydrogen peroxide, respectively. The results were calculated following the Wentworth scale for particle size classification.

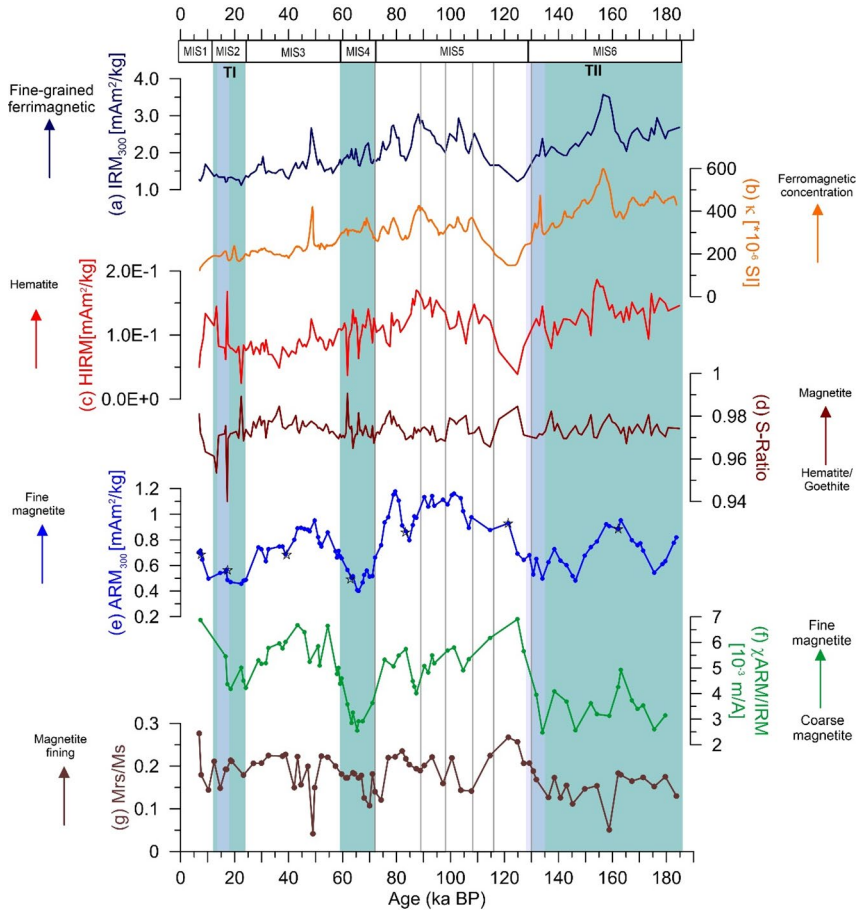

Figure 2. Downcore environmental magnetic parameters (a)–(f), and hysteresis parameter Mrs/Ms (g) from marine sediment core GL-1090. (a) IRM_{300}, (b) magnetic susceptibility (κ), and (c) HIRM, record changes in the concentration of magnetic minerals. (d) S-Ratio, records relative changes in magnetite versus haematite. (e) ARM_{300} reflects changes in the concentration of fine magnetic grains, (f) χARM/IRM, and (g) Mrs/Ms record changes in the relative proportion of fine magnetite *vs.* course magnetite. Black stars in plot (e) show the samples we performed FORC analysis. The main lithological changes vary accordingly with cold/warm stages, blue/white bars, respectively, which represent marine isotope stages (Lisiecki & Raymo, 2005). Gray lines represent the MIS 5 stages (Santos et al., 2017), and gray bars show Terminations II and I (TII and TI, respectively) (Lisiecki & Raymo, 2005).

4. Results

4.1. Magnetic Characterization

4.1.1. Magnetic Mineral Concentration

Magnetic susceptibility (κ) displays highest values (Figure 2b) during marine isotope stage (MIS) 6, reaching a prominent peak (~600×10^{-6} SI) at ~157 ka, and then gradually declining (except during MIS 4) through to the present interglacial (MIS 1). Some variability is evident during MIS 5; during the last interglacial (MIS 5e), magnetic susceptibility reaches its lowest values (~122×10^{-6} SI), comparable with the low values of MIS 1. At about 48 ka, it rises again (~414×10^{-6} SI); magnetic susceptibility is increased during the entire MIS 4, as we observe during MIS 6, but varies within a smaller range. IRM_{300} varies in accordance with magnetic susceptibility throughout the core (Figures 2a and 2b; Figure 6a), ranging between 1×10^{-3} and 4×10^{-3} Am^2/kg. HIRM follows the general trend of magnetic susceptibility and IRM_{300} (Figure 2c), with values ranging between 1×10^{-5} and 4×10^{-4} Am^2/kg (Figures 2a–2c). We calculated Pearson (ρ_p) and Spearman (ρ_s) correlation coefficients and a good correlation exists between HIRM and κ ($\rho_p = 0.64$ and $\rho_s = 0.67$). From MIS 6 to MIS 2, low but measurable HIRM values display similar variations as IRM_{300}.

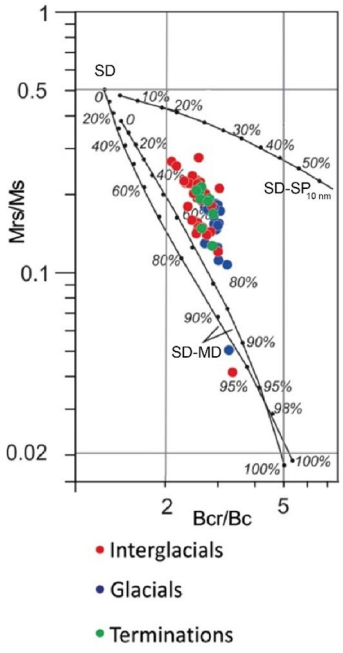

Figure 3. Magnetic hysteresis parameters from marine sediment core GL-1090 represented on a plot of Mr/Ms versus Bcr/Bc (Day et al., 1977). Samples collected in different climate periods are represented by red (interglacial), blue (glacial), and green (termination) circles. The data fields represent areas expected for single domain (SD), pseudo-single domain (PSD), and multi-domain (MD) (titano) magnetite particles. The curves represent theoretical mixing lines for SD–MD and SD-$SP_{10\ nm}$ mixtures (Dunlop, 2002).

Local HIRM maxima in MIS 1, however, indicate selective enrichment of high-coercivity minerals in these interglacial horizons.

4.1.2. Magnetic Mineralogy

The S-ratio mean value (~0.97) is close to the theoretical maximum of 1 for most of the studied period (Figure 2d). It is notable that the lowest S-ratio value (0.94) is observed at ~17 ka, at the same level as the ferruginous crust, and thus likely reflects the increased presence of oxidized magnetic minerals (Figure S7). In IRM acquisition curves, ~95% of the magnetization is saturated before 300 mT (Figure S5), indicative of magnetically soft magnetic minerals. The hysteresis loops all present similar shapes, with a narrow waist and low coercive fields ranging between 10 and 18 mT (Figure S6a). All samples show an important paramagnetic component (~70%) (Figure S6b). We calculated the mean coercivity from ARM demagnetization curve for 10 samples along core GL-1090, and the average value is ca. 27 mT.

4.1.3. Magnetic Grain Size

The hysteresis ratios Mrs/Ms and Bcr/Bc range from 0.1 to 0.3 and from 2.0 to 3.5, respectively (Figures 2g and 3). Using the Day Plot (Day et al., 1977) and following the theoretical SD-MD mixing curve proposed by Dunlop, 2002, our samples fall in the range of 40%–80% coarse MD grains (Figure 3). Grouping the samples into glacial (MIS 6, 4, and 2), transitional (glacial termination) and interglacial horizons (MIS 1, 3, and 5) reveals a trend of relative grain size fining from cold to warm stages. MIS 5, 3, and 1 show higher ARM_{300} values (higher concentration of finer, SD-like magnetic grains) relative to the cold MIS stages, 6, 4, and 2 (Figure 2e). Short-duration (millennial-scale) decreases in ARM can be seen during MIS 5d/5c and MIS 5b/5a transitions, and higher values during MIS 5e, 5c, 5a. Coeval variations both in χARM/IRM and Mrs/Ms further demonstrate a relative coarsening of the magnetic grain size during cold climate stages (Figures 2e–2g).

FORC diagrams for samples from each isotope stage are dominated by a central ridge feature, confirming the presence of non-interacting SD particles in each measured horizon. Separation of the central ridge (CR) from the background (BG) signal allows characterization of the SD and MD fractions (Figures 4 and S9). Figure 4 shows the extracted CR features and their normalized coercivity distributions. The topmost sample (4 cm depth) has the strongest signal, indicating highest SD magnetite concentrations. Its lower coercivity spectrum (average $H_c < 10$ mT) that is connected to the vertical ($H_c = 0$) axis suggests the presence of very fine particles close to the SP-SD threshold. All samples from below 4 cm core depth contain fairly similar CRs, indicative of stable SD grains. The similarity of the curves suggests that the properties (e.g., size and mineralogy) of the SD particles remain fairly constant below 36 cm depth.

4.2. Major Elements

The highest ln(Ti/Ca) values are observed in the first half of MIS 6 and during MIS 4 (Figure 5f). During MIS 5, this ratio shows several peaks between 110 and 106 ka (MIS 5d/5c transition), 91 and 85 ka (MIS 5b/5a transition), and ~79.6 and 77.2 ka (MIS 5a) (Figure 5f). Minima in ln(Ti/Ca) values are observed just after Terminations II (TII) and I (TI), during MIS 5e and MIS 1, respectively. A peak in ln(Fe/Ca) is observed at ~17 ka (not matched in prominence by the ln(Ti/Ca) ratio) (Figures S3a and S3b), which is probably related to the ferruginous crust (Figure S7) observed in this part of the core (for lithology details, see Section 3.1). Since Fe bound in (oxy-) hydroxides is highly reactive, it can be prone to post-depositional dissolution and re-precipitation; whereas Ti is resistant to alteration. Therefore, we use ln(Ti/Ca) as a conservative proxy for terrigenous input. Two significant peaks are also observed in ln(Fe/Ti) (~130 ka, during TII, and at ~17 ka, during TI) and an abrupt decrease during MIS 5e (Figure 5l).

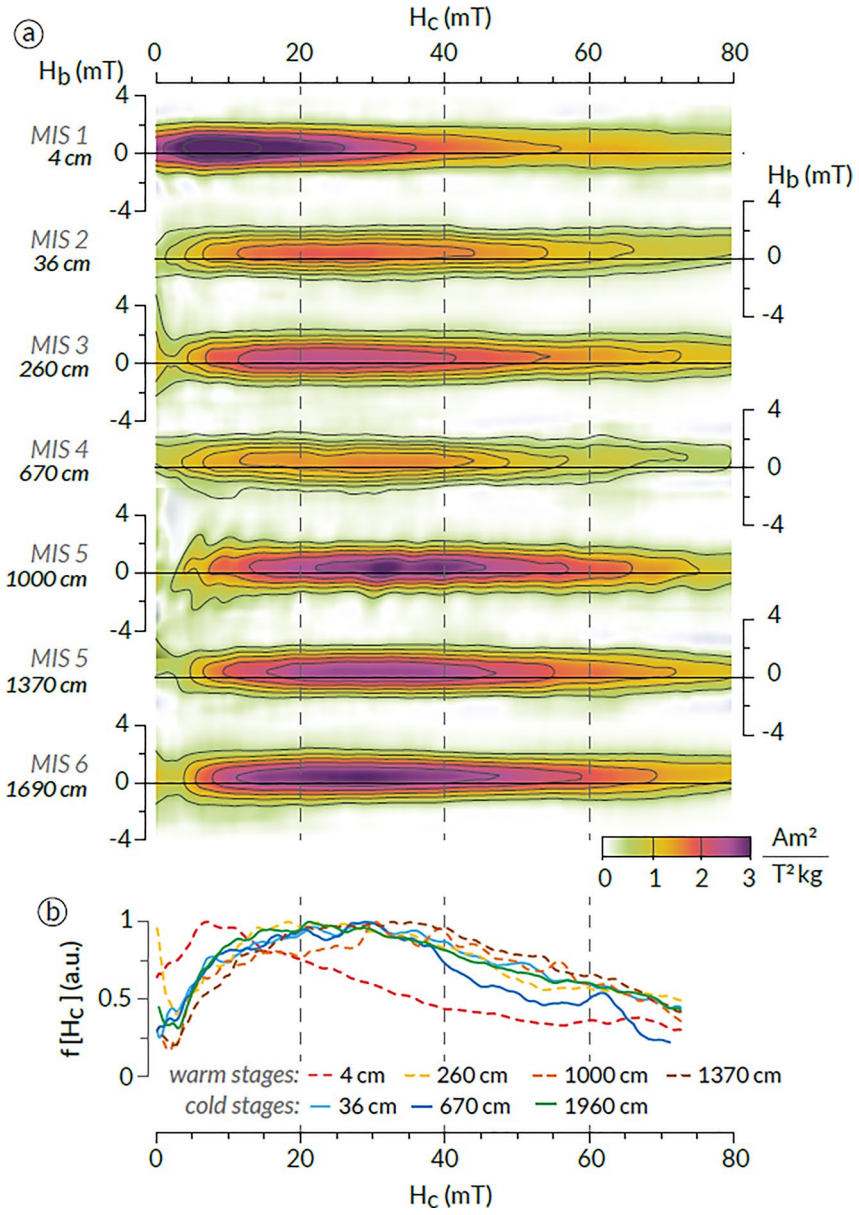

Figure 4. Down core series of FORC diagrams for representative samples from marine sediment core GL-1090. (a) Isolated central ridges, and (b) combined normalized coercivity distributions of the central ridges shown in panel (a). The respective Marine Isotope Stage (MIS) of each sample is indicated in the left-hand side of panel (a). For measurement and analytical detail see Section 3.3 of the text. Black stars in Figure 2e represent the location of the FORC samples along core GL-1090.

Values of ln(Fe/K) display little variability during most of the recorded period, except for two notable peaks (post-depositional feature) during TII and TI (Figure S3c). During TI, ln(Fe/K) values gradually increase, with a sharp drop at the end of the termination, followed by another gradual increase up to MIS 1. To avoid the influence of the outliers we observe in Fe/K (Figure S3c), we used K/Ti instead to examine sediment source. The ln(Al/Si) values show little change during MIS 6, a sharp increase just after TII, a gradual decrease encompassing MIS 5-2, and a sharp increase just after TI (Figure 5j). Aiming to evaluate the marine contribution (i.e., biogenic opal), we also present the ln(Al/Ti), which reflects only the terrigenous input (Figure S3d). The correlation between ln(Al/Ti) and ln(Al/Si) is high ($\rho_p = 0.81$) during MIS 6-4, but after that ln(Al/Ti) shows a smooth decrease during MIS 3, whilst ln(Al/Si) exhibits few variance (Figure S2b).

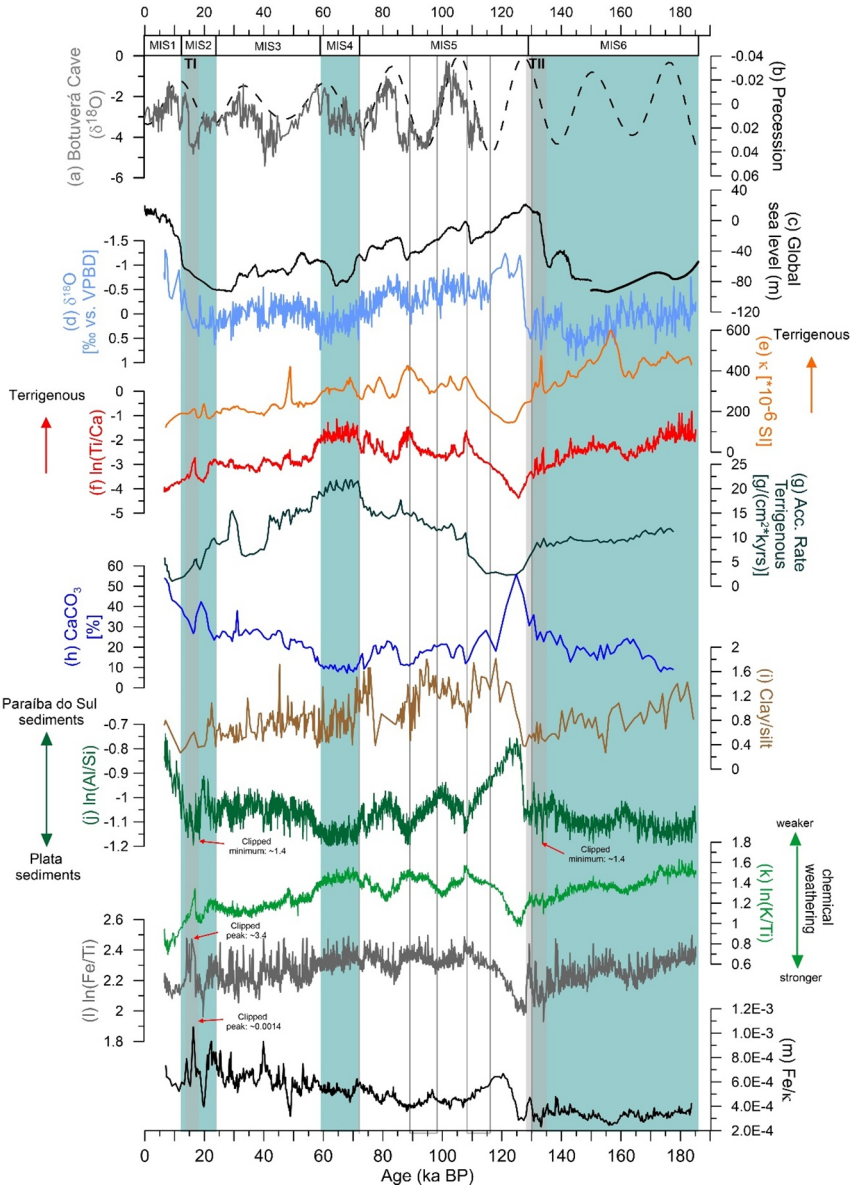

Figure 5. Downcore parameters from marine sediment core GL-1090. External literature: (a) Speleothem $\delta^{18}O$ from Botuverá Cave (Cruz et al., 2006), (b) Precession (Berger & Loutre, 1991), (c) Global Sea Level for the last 150 (Grant et al., 2012) and between 150 and 186 ka (de Boer et al., 2012), (d) *Globigerinoides ruber* $\delta^{18}O$ (Santos et al., 2017), and (h) $CaCO_3$ (%) (Figueiredo et al., 2020); parameters for sediment provenance: (e) magnetic susceptibility, (f) Ti/Ca, (g) accumulation rate of terrigenous, (i) Clay/Silt, (j) Al/Si, (k) K/Ti, and reductive proxies: (l) Fe/Ti and (m) Fe/κ. The main lithological changes vary accordingly with cold/warm stages, blue/white bars, respectively, which represent marine isotope stages (Lisiecki & Raymo, 2005). Gray lines represent the MIS 5 stages (Santos et al., 2017), and gray bars show Terminations II and I (TII and TI, respectively) (Lisiecki & Raymo, 2005).

Notable features of the Fe/κ data are a sharp increase just after Termination II, a marked decrease prior to Termination I, and an increasing trend until MIS 1, when it declines (Figure 5m).

4.3. Redox-Sensitive Elements

Under suboxic to anoxic conditions, Mn, Fe, and S can easily be remobilized in the sediment. Relative enrichment and depletion of Mn and Fe can, therefore, reveal insights into the sediment redox conditions and bottom water oxygen concentration during deposition (Reitz et al., 2004). In core GL-1090, prominent

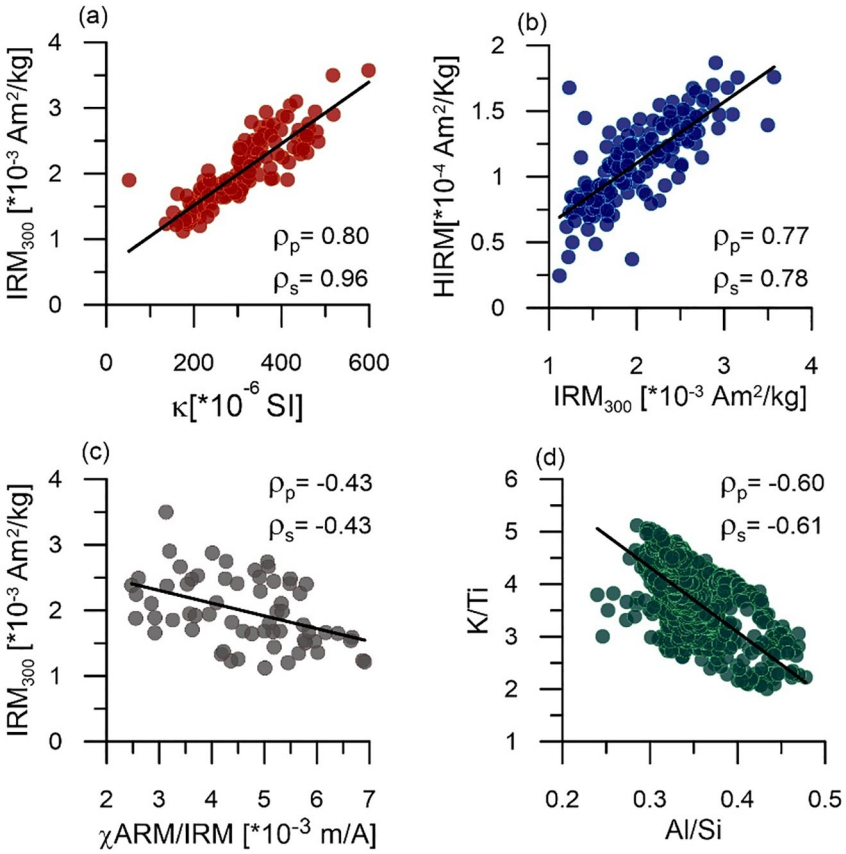

Figure 6. Scatterplots between magnetic and geochemical proxies from marine sediment core GL-1090. The black line represents the linear fit. Pearson Correlation Coefficient (ρ_P) and Spearman Correlation Coefficient (ρ_S) were calculated and are displayed on the plots.

anomalies in ln(Mn/Ti) and ln(Fe/Ti) relative to core-top values reveal a characteristic sequence of Mn and Fe enrichment at two levels (Figure 7). Consecutive peaks of these two trace metals at the end of MIS 2 and MIS 6 for Fe and just after that at MIS 5e and MIS 1 for Mn correspond to the last two glacial terminations (Figure 7). During TII and TI ln(Fe/Ti) peaks likely reflect the post-depositional iron re-precipitation in the ferruginous crust, with no peak seen in the ratio ln(K/Ti) (Figures 5k and 5l). Likewise, an abrupt decrease in ln(Fe/Ti) after TII leading to a pronounced minimum during MIS 5e indicates Fe depletion. In contrast to Mn and Fe, we find only minor variations in relative S concentration (ln(S/Ti), Figure 7).

4.4. Siliciclastic Grain Size

The sediment in core GL-1090 is mainly composed of mixed silt and clay, with minor contribution of sand (<1%) detected only in four samples. The clay/silt ratio ranges between 1.81 and 0.27 (Figure 5i). A gradual reduction in the clay/silt ratio is observed during MIS 6 and from MIS 4 to MIS 1, indicating a decrease in the proportion of the finest particles, reaching a minimum around both TII and TI (0.37 and 0.36, respectively). A marked rise in the clay/silt ratio is observed during MIS 5e; the predominance of fine sediments is maintained during MIS 5d, 5c, 5b, and also during the transition from MIS 5a to MIS 4.

5. Discussion

5.1. Sediment Composition Controlled by Source Area and Sea-Level

The magnetic concentration parameters (IRM_{300} and κ) alongside ln(Ti/Ca) indicate the highest terrigenous inputs during MIS 6 (~160 ka) and transitions MIS 5d/c (~108 ka) and b/a (~90 ka), and the lowest during

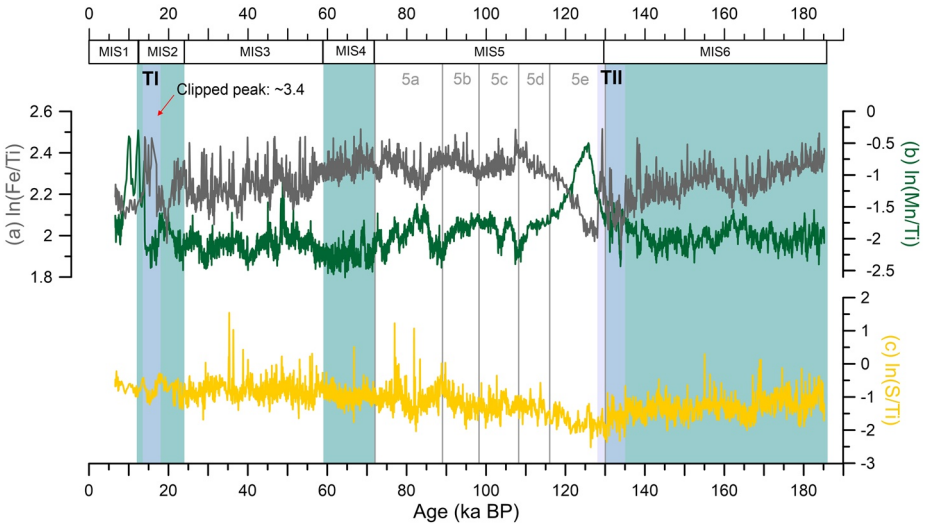

Figure 7. Redox sensitive elements represented by relative iron (Fe/Ti), magnesium (Mn/Ti), and sulphur (S/Ti) concentration compared to the terrigenous "background sedimentation" represented by titanium. The main lithological changes vary accordingly with cold/warm stages, blue/white bars, respectively, which represent marine isotope stages (Lisiecki & Raymo, 2005). Gray lines represent the MIS 5 stages (Santos et al., 2017), and gray bars show terminations II and I (TII and TI, respectively) (Lisiecki & Raymo, 2005).

MIS 5e and 1 (Figures 2a, 5e, and 5f). Both IRM_{300} and κ are dominated by a ferrimagnetic (magnetite-like) mineral component. Comparatively low HIRM and high S-ratio values suggest only minor contributions from antiferromagnetic minerals (hematite and/or, less likely, goethite) (Figures 2c and 2d). Because HIRM follows the general trend of IRM_{300} and magnetic susceptibility its changes may also reflect variations in the concentration of ferrimagnetic particles, instead of variance in the type of magnetic minerals (Figure 6b). The concentration of fine-grained magnetite, represented by ARM_{300} (Figure 2e), does not mirror variations in IRM and susceptibility, but instead exhibits maxima during warm stages MIS 3 and MIS 5. The magnetic grain size proxy χARM/IRM (Figure 2f) varies accordingly, indicating a relative enrichment in single domain magnetite in interglacial stages.

High values of magnetic susceptibility, ln(Ti/Ca) and the accumulation rate of terrigenous material during MIS 6 and 4 reflect an increase in terrigenous supply and a possible response to glacio-eustatic sea-level fall (Figures 5e–5g, 6a, 6b, and S2d). These changes in terrigenous supply are accompanied by compositional changes as evident from variations in ln(Al/Si) and ln(K/Ti) (Figures 5i and 5j, 6d, S2f and S2g). The correlation between ln(K/Ti) and ln(Ti/Ca) demonstrates that the siliciclastic sediment composition is closely linked to the amount of terrigenous material deposited. A more acid geochemical signature (elevated K/Ti and reduced Al/Si) corresponds to a larger terrigenous fraction (Ti/Ca). Notably, the S-ratio is consistently high throughout core GL-1090, and shows no covariation with either proxies sensitive to changes in terrestrial chemical weathering (K/Ti and S-ratio show low correlation and is not shown here; $\rho_p = 0.05$ and $\rho_s = 0.12$) nor with precipitation records from SE South America (Cruz et al., 2005, 2006). Thus, in contrast to the siliciclastic sediment composition, the sediment magnetic mineralogy type has remained constant over time (Figures 2, 5a, and S2h).

Long-term changes in precipitation over SE South America have been attributed to orbital-scale variations in insolation (directly affected by precessional changes) (Figures 5a and 5b). Precipitation over southeastern South America is associated with the mature phase of the South America Monsoon System (Marengo et al., 2012), which is characterized by a well-developed South Atlantic Convergence Zone (Carvalho et al., 2004). The Plata and Paraíba do Sul drainage basins are under the influence of the South America Monsoon System, which produces a see-saw effect: enhanced (decreased) precipitation in its core and the southern Brazilian coast, and drier (wetter) conditions in southern South America (Garreaud et al., 2009). During austral summer, maximum insolation in the Southern Hemisphere (sub)tropics intensified the monsoon system , increasing the relative amount of summer precipitation (Cruz et al., 2005). Changes in

terrigenous content (magnetic susceptibility, IRM_{300}, HIRM, ln(Ti/Ca), ln(Al/Ti)) and weathering product (ln(Al/Si) and ln(K/Ti)) of core GL-1090 do not follow changes in precession (Figures 2, 5, and S2g, S2i, S2j). Thus, we exclude precipitation as a controller for terrigenous input in our study site.

Variations in ln(Al/Si) have been used to track changes in siliciclastic particle size (Mulitza et al., 2008), in circumstances where there have been no major changes in terrestrial chemical weathering conditions or the flux of biogenic opal (Chiessi et al., 2010). The siliciclastic particle size distribution in GL-1090 gradually changes from clay- to silt-dominated from early to late MIS 6, reaching its maximum coarseness during Termination II and I (Figure 5m). After TII, and in association with maximum sea-level (i.e., MIS 5e), particle size becomes finer, until clays dominate the record. Notwithstanding a similar trend in siliciclastic grain size and ln(Al/Si) across Termination II, overall, the correlation between both parameters is not significant (Figure S2e); thus, siliciclastic grain size appears not to be the main driver of variations in the Al/Si ratio in core GL-1090. Concerning biogenic opal, some authors have suggested an increase in silicic acid content and primary productivity in the southern Brazilian margin during cold stages (Portilho-Ramos et al., 2019). However, the concentration of biogenic opal at ~2,000 m water depth, the depth of our core site, is small (<1%) according to Romero and Hensen (2002).

The parameter Fe/κ varies coevally with ln(Al/Si) and with sea-level changes (Figures 5c, 5j, and 5m; $\rho_p = 0.85$, scatterplot not presented). Changes in Fe/κ may reflect post-depositional Fe remobilization (Funk et al., 2004; Reitz et al., 2004), as seen in the Fe enrichment, in association with the ferruginous crust in core GL-1090 (Figure S7), and/or changes in terrigenous source materials, with differing proportions of para- and ferromagnetic Fe-bearing minerals (Itambi et al., 2009). Because of the covariation of Fe/κ with the redox independent parameter (Al/Si), we infer that overall Fe/κ reflects changes in the primary Fe-oxide mineralogy. Coeval minima in ln(Al/Si) and Fe/κ suggests that relatively more Fe was bound in ferromagnetic minerals of the sediment delivered to our core site (Figures 5j and 5m).

Temporal changes in Al/Si may indicate variation in the source weathering conditions. Al enrichment, recorded during interglacial periods (MIS 1 and 5e), thus points to either enhanced weathering in the source area and/or to a shift in sediment source toward more humid areas in proximity to the core location. A typical weathering product in tropical regions is the Al-rich clay mineral, kaolinite. Originating predominantly from NE Brazil, kaolinite constitutes more than 80% of the clay mineral fraction at ~20°S (off the Paraiba do Sul River mouth) and to less than 10% off the Plata River, south of ~30°S (Petschick et al., 1996). In arid regions, weathering can lead to potassium (K) enrichment (from illite or K-feldspar); in the surface sediments of the western South Atlantic, K enrichment is expressed as a strong south-north gradient in ln(K/Ti) values (Figure S4c). The observed anti-correlation between ln(Al/Si) and ln(K/Ti) in GL-1090 further supports a shift between more humid weathering products deposited during interglacial periods and more arid weathering products deposited during glacial periods.

There is very little riverine input to the continental margin off southeastern Brazil, thus contributions from more distal areas with higher runoff seem likely. Several studies have shown that at sea level lowstand, a substantial fraction of the terrigenous material from the Plata River plume reaches as far north as 24°S (Gyllencreutz et al., 2010; Mathias et al., 2014; Piola et al., 2000, 2005). Magnetic characterization of modern Plata River sediments identified the presence of ultrafine and fine (4–16 μm) detrital magnetite in the Plata mud belt, that would be transported up to 24°S by the BCC (Razik et al., 2015). The influence of Plata River sediments at this latitude was also suggested for the mid-Holocene based on environmagnetic parameters (Mathias et al., 2014). In addition, the elemental composition of suspended sediment from the Plata River exhibits the same Al/Si values as measured in sediments from the south Brazilian margin (24°S) (Depetris et al., 2003). Paraíba do Sul River is another potential source area to the Southeastern South America adjacent margin. In the surface sediments of the Western South Atlantic, the Al/Si ratio (as well as the kaolinite concentration) exhibits a strong latitudinal gradient (Govin et al., 2012; Petschick et al., 1996) (Figure 1c). Govin et al. (2012) have found comparable Ti/Al values between south Brazil (24°S–38°S) and Plata River sediments. We observe a good correlation between ln(Al/Si) and ln(Al/Ti) in MIS 6-2 ($\rho_p = 0.84$ and $\rho_s = 0.73$) in core GL-1090 (Figure S2b), which may suggest an enhanced supply of Plata River-sourced sediment during glacial stages. As biogenic opal does not affect Al/Ti, we assume that the influence of biogenic opal on the ln(Al/Si) record is negligible. Mn/Ti ratios along core GL-1090 show a peak in Termination I that clearly reflects changes in the redox condition, since it happens just after the Fe peak (Figures 7a and

7b). In TII, there is a less clear peak, possibly reflecting a mixing signal; redox conditions plus sediment from volcanic rock in Paraná Basin. After TII and TI, sudden increases in ln(Al/Si) likely reflect decreased delivery of Plata River sediments to our study site. Transgressive sea-level events drowned the Plata River estuary, decreasing the northwards transport of Plata River sediments by the BCC. During these periods, the reduction in Al-rich siliciclastics indicates a changed and/or additional sediment source, producing a mixture of sediments from the Plata and Paraíba do Sul rivers. We therefore suggest that relative Al depletion and K enrichment during full glacial stages MIS 6, 4 and 2 (and, to a lesser degree at the MIS 5d/5c and MIS 5b/5a transitions) reflect the northward extent of the Plata River plume, modulated by glacio-eustatic sea-level changes. Minimum ln(Al/Si) and maximum ln(K/Ti) values in GL-1090 indicate that terrigenous sediments delivered to our study site during glacial periods were similar in composition to present day surface sediments deposited off the Plata River mouth. We therefore infer that the Plata plume was the dominant source of terrigenous sediment to our study site during glacial maxima. A reduced northward transport of the Plata plume during interglacial sea-level high stands led to an overall decrease in terrigenous input to the study site, promoting a higher relative contribution from Paraíba do Sul River.

Additional to the suspended sediments from the Plata and Paraíba do Sul rivers, another potential source of terrigenous sediments is aeolian dust transported by the westerlies to the Argentinean and Uruguayan continental shelves (e.g., Maher et al., 2010). Prospero et al. (2002) characterized three main dust sources in South America: one located in the Bolivian Altiplano (20°S, 67°W) and two in Argentina: Patagonia (38–48°S) and Santa Cruz (46–48°S). These authors identified a modern active dust area in the southern Pampas and northern Patagonia. According to Gaiero et al. (2003), about 90% of the present day material deposited in the SW South Atlantic is delivered by the atmospheric pathway and comes from Patagonia. The magnetic characterization of sediments from the southeastern Brazil margin (24°S) indicates the Argentinean loess as the possible source of fine magnetite (PSD) between 6 and 4.7 ka BP (Mathias et al., 2014). In addition to the Plata Plume sediment, Razik et al. (2015) suggested that material delivered to the Southern Atlantic margin from the Argentinean Pampas by westerly winds is transported further north (24°S) as well. These authors reported magnetic concentrations in surface sediments that are widely different from the magnetic data from core GL-1090 (Figure S8). Especially the magnetic grain size parameter (χARM/IRM) from core GL-1090 is one order of magnitude higher than the surface sediment data from Southern Atlantic margin, whereas the other magnetic parameters present similar values with the Pampean Shelf magnetic material, which is mostly composed of aeolian dust transported by the westerlies.

5.2. Terrigenous versus Biogenic Signals

Similar to the geochemical proxies for terrigenous sediment input (Ti/Ca and K/Ti), the magnetic mineral concentration (as indicated by IRM_{300} and κ) is greatest during MIS 6 (~160 ka) and transitions MIS 5d/c (~108 ka) and b/a (~90 ka), and lowest during MIS 5e and 1 (Figures 2a–2c and 5e, 5f, 5k). In contrast, the concentration of the magnetic fine fraction (ARM and χARM/IRM, Figures 2e and 2f) shows low correlation with total terrigenous flux to our study site (Figures 6c and S2c). Continuous S-ratio values close to 1 throughout the core (Figure 2d), together with >95% IRM acquisition at fields smaller than 300 mT (Figure S5), indicate that the sediment magnetization is carried by a magnetically soft material like magnetite (or potentially greigite). Substantive contributions from greigite, a common authigenic magnetic Fe-sulphide, can however be excluded because of the absence of its characteristic signatures from the FORC diagrams (Figures 3 and 4) (Roberts et al., 2006). Thus, it appears that the magnetic remanence is dominantly carried by magnetite throughout core GL-1090.

Alongside ARM, both magnetic grain size-dependent parameters (χARM/IRM and Mrs/Ms) indicate enrichment of SD magnetite in the warm stages MIS 1, 3, and 5 and depletion in the cold stages MIS 2, 4 and 6 (Figures 2e–2g). Considering domain state estimates from the Day plot (Day et al., 1977) our data fall in two clusters in the area characteristic for PSD particles or of SD-MD mixtures of ~40%–80% MD particles (Day et al., 1977; Dunlop, 2002). HIRM and S-ratio show no correlation, which suggest that minor hematite inputs observed along core GL-1090 are independent from magnetite enrichment (Figures 2c, 2d, and S2d). Magnetic grain size (χARM/IRM) plotted against the concentration parameter IRM_{300} shows anti-correlation, implying that the SD magnetite fraction changes independent of terrigenous flux (Figures 2

and 6c). This indicates either an additional source of SD magnetite during warm stages and/or selective dissolution of the fine fraction during cold stages.

FORC diagrams of all samples of core GL-1090 are dominated by a central ridge, which indicates the presence of non-interacting SD particles (Egli et al., 2010) throughout the core (Figure 4a). The low Hc central ridge in the 4 cm sample (MIS 1) may suggest an assemblage of nanometre-sized less stable particles close to the SP-SD threshold (10–15 nm), possibly extracellular magnetite (Lovley et al., 1987; Roberts et al., 2000). Potentially this particle fraction is absent below 4 cm depth because of reductive dissolution (Hounslow & Maher, 1999). The coercivity range (30–40 mT) of the central ridge from our samples below 4 cm depth has been reported previously as a typical signal of bacterial magnetite (Egli et al., 2010; Roberts et al., 2012). Low (32–44 mT) and restricted coercivity range has been attributed to uniform grain size assembly of MTB magnetite (Abrajevitch & Kodama, 2011). Similar coercivity has been observed also in silicate crystals with magnetite inclusions (Chang, Roberts et al., 2016). The presence of fine magnetite (SD) from clayey silt weathered from La Plata Drainage Basin was detected up to 24°S along the Brazilian coast (Razik et al, 2015). Yet, a comparison between these data and our magnetic parameters shows that the concentration parameters κ, HIRM, and IRM_{300} from core GL-1090 are lower than most of the data from Razik et al. (2015), whereas some samples from the Plata Shelf display similar values (Figures S8a and S8b). In addition, our magnetic grain size parameter is an order of magnitude higher than the finest fraction identified by Razik et al. (2015), suggesting finer magnetic particles in core GL-1090 (Figure S8c). Regarding a partial dissolution of SD magnetite, it cannot be ruled out entirely. However the two facts that ARM minima are not restricted to the narrow horizons of Fe and Mn-mobilization and that we see no indication of enhanced sulfidization of the sediments (see 5.3), lead us to infer that reductive dissolution of the detrital magnetic mineral assembly was not important in core GL-1090. Greigite magnetosomes also have a central ridge, but typically show a lower coercivity range (maximum intensity~20 mT) (Chang, Vasiliev, et al., 2014; Chen et al., 2014; Reinholdsson et al., 2013). Hence, the SD particles detected here are consistent with magnetite magnetofossils.

The intensity of the FORCs central ridge varies following ARM intensity, suggesting that ARM primarily reflects the concentration of non-interacting SD magnetite (Figures 2e and 4a). If reductive dissolution would have affected the SD magnetite assemblage in some horizons selectively, one could expect an impact on the grain size distribution where SD concentrations are lowest. Identical coercivity distributions below 4 cm depth however suggest a uniform size distribution of the SD particles, further supporting the assumption of an ARM signal that was not affected by early diagenesis. The "background" FORC distributions with the central ridge removed are typical for PSD-MD ferrimagnetic particle assemblages (Roberts, 2006; Roberts et al., 2000). With highest intensities around H_C = 10 mT, we attribute the background FORCs to the detrital magnetite fraction (Figure S9). The uniform coercivity distribution among the background FORCs for GL-1090 samples suggests a consistent detrital magnetite component throughout the core.

Our environmagnetic parameters show that detrital magnetite is the dominant magnetic mineral in GL-1090 and variations in the magnetite concentration correspond to changes in the terrigenous flux. In contrast, the concentration of SD magnetite appears to be decoupled from the terrigenous flux. Significantly higher SD contribution in comparable surface sediments along the western South Atlantic (Razik et al, 2015) and the lack of evidence for selective dissolution of the fine fraction indicate that SD magnetite in core GL-1090 is derived from an independent, possibly post-depositional, process. Although not unique, the magnetic properties of the SD fraction are consistent with the presence of biogenic magnetite formed by magnetotactic bacteria.

5.3. Redox Conditions and Early Diagenesis Processes

To better understand the impact of any post-depositional alterations on core GL-1090 and its rock magnetic properties, we look at the distribution of reactive metal species that can give insights into the early diagenetic redox processes in the sediment. The redox conditions of sediments are driven by the microbial oxidation of organic matter (early diagenesis), as controlled by the balance between organic matter supply and the availability of oxidants. When oxygen is depleted, different types of microorganisms will utilize successively less efficient oxidants: nitrate, Mn-oxides, Fe-oxides and sulphate (e.g., Canfield & Thamdrup, 2009). Thereby, dissolved Mn^{2+} and Fe^{2+} can then migrate within the sediment column and

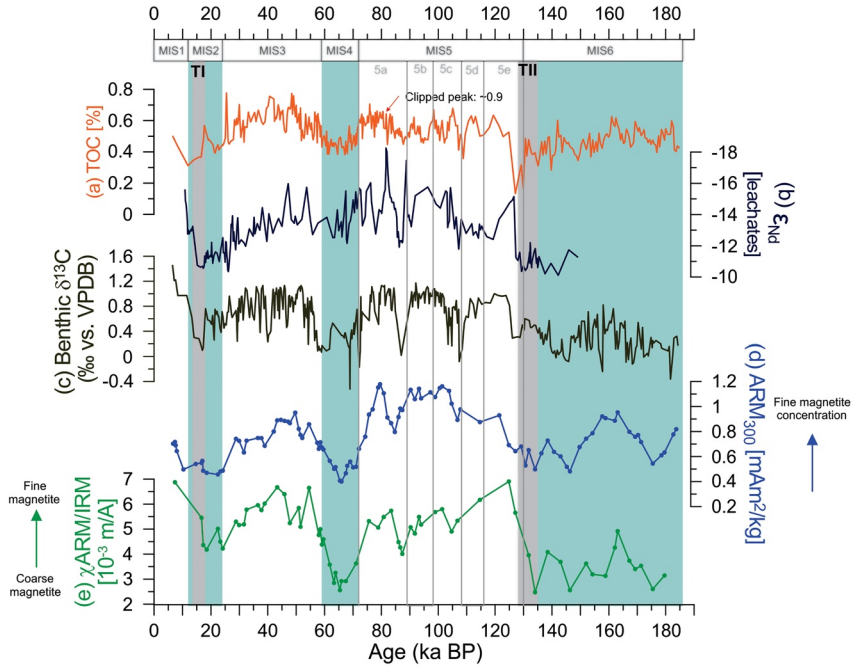

Figure 8. Association between SD biogenic magnetite and NADW ventilation via magnetic parameters, total organic carbon (TOC), stable carbon isotopic composition ($\delta^{13}C$) of benthic foraminifera and ε_{Nd} record. (a) TOC (Figueiredo et al., 2020), (b) ε_{Nd} record from Bermuda Rise ODP site 1,063 (Bohm et al., 2015) (c) benthic *Cibicides wuellerstorfi* $\delta^{13}C$ (Santos et al., 2017), and (d)–(e) magnetic grains size parameters from GL-1090. The main lithological changes vary accordingly with cold/warm stages, blue/white bars, respectively, which represent marine isotope stages (Lisiecki & Raymo, 2005). Gray lines represent the MIS 5 stages (Santos et al., 2017), and gray bars show terminations II and I (TII and TI, respectively) (Lisiecki & Raymo, 2005).

rapidly re-precipitate in the presence of oxygen or dissolved sulphide. Sudden changes in the availability of involved substances can cause an imbalance in the early diagenetic sequence. Such nonsteady state conditions can lead to the prolonged fixation of sediment redox zones and to localized accumulation of authigenic precipitates (Reitz et al., 2004).

Successive Mn and Fe enrichments associated with both glacial terminations in GL-1090 (Figure 7) are characteristic for a prolonged fixation of sub-oxic redox boundaries and indicate repeated non-steady state conditions (Reitz et al., 2004). Non-steady state conditions can be caused by a decrease in sedimentation rates, a decrease of bottom water oxygenation and/or an increase in bioavailable organic matter buried in the sediment (e.g., due to increase in primary productivity). The glacial terminations in GL-1090 are both associated with a drop in sedimentation rates (Santos et al., 2017), relative increase in carbonate (low ln(Ti/Ca), Figures 5f, 5g, and 5h) and minima in the TOC content (Figure 8a, Figueiredo et al., 2020). We thus suggest that the fixation of redox horizons at our study site was driven by the sudden decline of terrigenous sediment flux during glacial terminations. Reduced TOC concentrations at these horizons may be related to enhanced in situ carbon degradation during these times. Notably, Figueiredo et al. (2020) have reported anomalies in mercury (Hg) concentration in GL-1090 associated with the glacial terminations. They attributed these anomalies to changes in organic carbon cycling and, in case of TII, to the presence of an active redox boundary.

The maximum depth of the Fe peak at TI corresponds to the visually observed reddish-brown ferruginous crust (Figure S7) and likely represents the position of the present-day Fe-redox boundary (Fe^{2+}/Fe^{3+}). The successive Mn and Fe peaks at TII are less well defined than those around TI (Figures 7a and 7b). They likely represent a relic of non-steady state diagenesis during the rapid transitions from glacial conditions in MIS 6 to interglacial conditions in MIS 5e, analogous to the last glacial termination. The correlation between Al/Si and Mn/Ti is intermediate ($\rho_p = 0.58$ and $\rho_s = 0.54$; Figure S2i). Hence, the use of Mn/Ti as a proxy for sediment provenance is not reliable. Instead, we use Al/Si and K/Ti.

Local peaks in Fe/κ, that match anomalous ln(Fe/Ti) values during TII and TI, point to additional Fe remobilization effects (Figures 5l and 5m). The paramagnetic Fe component in these sediments is contributed by the clay minerals, biotite and nontronite. Notable is that the magnetic concentration-based parameters (IRM_{300} and HIRM) do not exhibit anomalies during TII and TI, suggesting that, notwithstanding some evidence of post-depositional Fe mobilization, the ferromagnetic signal along core GL-1090 appears to be preserved (Figure 2). In order to evaluate if the ferromagnetic signal has not been erased, and hence still reflects changes in sediment supply/provenance, we used elemental ratios excluding iron, ln(K/Ti) and ln(Al/Ti) (Figures 5k and S3d). Indeed, both of these ratios also undergo substantial changes during and after TII and TI, supporting an important shift in sediment provenance through the transitions MIS 6/5e and MIS 2/1.

The absence of sulphur enrichments at these horizons (associated with both glacial terminations) furthermore demonstrates the oxic character of the Fe-precipitates (Figure 7). The general absence of localized S enrichments in the core indicates that either suboxic (nonsulfidic) reduction prevailed in the sampled horizons or that the sulfidic zone has not been fixed at a certain depth interval. This assumption is further supported by the observation that none of our rock magnetic proxies show depletion zones, even in horizons where there is evidence for Fe-mobilization. Possibly, an excess of more readily soluble Fe-oxyhydroxides played a role in the preservation of magnetite. Ferrihydrite, for instance, has been suggested to be more reactive toward sulphide than iron oxides (Canfield, 1989). Such minerals may have been preferentially dissolved and remobilized leaving the distribution of the more crystalline magnetic Fe-oxide fraction intact.

Given that Fe remobilization is limited and does not appear to control the preservation of the ferromagnetic signal (Figures 2 and 5e), we suggest that our SD magnetite-sensitive parameters reflect climatically modulated changes in the rate of biogenic magnetite formation (Figures 8d and 8e). We cannot exclude the alternative possibility of selective biogenic magnetite dissolution/preservation but some observations argue against magnetite dissolution in the cold stages when SD magnetite concentration is low. The redox sensitive proxies, Fe/Ti and Fe/κ, indicate that horizons associated to glacial terminations experienced Fe remobilization, which likely involved the local dissolution of Fe-oxides. However, minima in SD magnetite are not restricted to these narrow horizons but occur throughout the entire cold stages MIS 6, 4 and 2. As we find no indication for the systematic dissolution of magnetite in these cold stages, it appears reasonable to assume that variations in SD magnetite reflect the primary concentration of SD magnetite.

5.4. Magnetite Formation Induced by Mid-depth Ventilation

ARM is very sensitive to the presence of SD magnetite particles (Evans & Heller, 2003; Maher, 1988; Schmidbauer & Veitch, 1980). SD magnetite exhibits ARM 1–2 orders of magnitude higher than the larger MD magnetite (Dunlop, 1981; Hartstra, 1982; Maher, 1988; Peters & Dekkers, 2003). Within sedimentary sequences, the presence of biogenic intracellular magnetite records the past activity of MTB (Funk et al., 2004; Kirschvink & Chang, 1984; Kopp & Kirschvink, 2008; Korff et al., 2016; Petersen et al., 1986; Stolz et al., 1986; Vali et al., 1987). MTB actively form well-ordered chains of magnetite (or more rarely, greigite), often as uniform SD particles (Bazylinski, 1999; Bazylinski et al., 1995; Blakemore et al., 1985; Matsuda et al., 1983). Upon deposition and preservation within sediments, these particles, released by lysis of the host magnetosomes, form a fossil record of past MTB activity, physical characteristics that allow them to be identified by their strong and distinctive magnetization (Egli et al., 2010; Maher & Hounslow, 1999; Roberts et al., 2012, 2013). The magnetofossil concentration depends on (i) the MTB abundance, thus magnetite production during sediment deposition, and (ii) the degree of preservation of SD magnetite crystals released from magnetosomes after burial. Reductive dissolution of iron oxides includes the removal of authigenic magnetic minerals (including biogenic magnetite) from the sediment and may eliminate the magnetofossils (Chang, Bolton, et al., 2016; Korff et al., 2016; Lippert, 2008; Maher & Hounslow, 1999). Thus, water column conditions, early diagenesis and all post-depositional processes that may affect the microbial metabolism (i.e., surface primary productivity, carbon exported to the seafloor, organic matter decomposition) can all play a role in the preservation or dissolution of these magnetofossils.

The concentration of biogenic magnetite in sediments can mirror the past abundance of MTB during the time the sediment formed. However, due to their small size, magnetofossils are also susceptible to reduc-

tive dissolution and their abundance may respond to post-depositional redox processes. As outlined above, we find no indication for glacial-stage dissolution of SD magnetite in GL-1090. Korff et al. (2016) reported characteristic coarsening of magnetite in pelagic sediments affected by dissolution, with correlation between magneto-granulometric parameters (ARM_{300}, χARM/IRM) and concentration-dependent parameters (κ and IRM), and with Fe. Core GL-1090 displays no such correspondence between these parameters, suggesting that little or no dissolution effects took place (Figures 7c and S2c). Further, the interplay between MTB production/preservation and organic carbon flux can provide valuable insights into diagenetic conditions in the sediment. Roberts et al. (2011) have shown that higher organic carbon concentration is associated with greater MTB abundance. Here, TOC changes are generally coeval with magnetic grain size fining, with low (high) values during the glacial (interglacial) horizons (Figures 8a, 8d, and 8e). The correlation between TOC and benthic $\delta^{13}C$ shows intermediate values, due to the different trends in TII and TI (Figures 8a and S2k). Without these outliers, represented by low TOC (%) values, the TOC/benthic $\delta^{13}C$ correlation increases to $\rho_p = 0.56$ and $\rho_s = 0.58$. Hence, it seems likely that the middepth site of core GL-1090 in the subtropical western South Atlantic was propitious for MTB production under interglacial and glacial conditions during the last ~184 ka, with enhanced (decreased) MTB production during warm stages (glaciations), but no cessation of bacterial magnetite formation during the lower-oxygen glacials (Figures 8a, 8d, and 8e).

Association between scavenging of reactive species of metal and physical/chemical conditions of NADW has been found recently by Figueiredo et al. (2020), supporting the idea of bottom water ventilation affecting sediment redox conditions in the subtropical western South Atlantic. The negative excursions in benthic $\delta^{13}C$ in core GL-1090 core suggest that bottom water ventilation changed at this site during the last ~184 ka. Notably, the concentration of fine-grained magnetite (ARM_{300}) and the grain size-dependent parameter (χARM/IRM) co-vary with $\delta^{13}C$ of epibenthic foraminifera *Cibicides wuellerstorfi* (Santos et al., 2017), indicating that common processes may have controlled these parameters (Figures 8c–8e and S2l). It is notable that both our SD magnetite record and $\delta^{13}C$ anomalies from core GL-1090 (Santos et al., 2017) vary synchronously with ε_{Nd} from Bermuda Rise sediments (Bohm et al., 2015) (Figure 8b) reinforcing the notion that middepth ventilation plays a key role in ocean variability over different timescales through changes in the Atlantic Meridional Overturning Circulation strength. Changes in in the abundance of benthic microbes, like MTB, may also be related to varying conditions in the overlying bottom water. Since $\delta^{13}C$ of *C. wuellerstorfi* reflects the $\delta^{13}C$ of the bottom water dissolved inorganic carbon with no pore water effects (Mackensen et al., 1993; Mackensen & Schmiedl, 2019), we suggest that MTB magnetite production was at least partially controlled by changes in the overlying bottom water. Negative $\delta^{13}C$ excursions in the western South Atlantic are frequently associated with periods of weak Atlantic Meridional Overturning Circulation (e.g., glacial stages and Heinrich stadials) (Campos et al., 2020; Lund et al., 2015; Santos et al., 2017; Schmittner & Lund, 2015). During these periods of reduced ventilation, increased NADW residence time allowed the accumulation of respired carbon at Atlantic mid-depths (Campos et al., 2020; Howe et al., 2016; Schmittner & Lund, 2015; Voigt et al., 2017). The carbon accumulated as a result of increased microbial respiration at the expense of oxygen. Seawater $[O_2]$ reconstruction from the North Atlantic also points to a decrease in the oxygen availability of bottom waters during cold events (Hoogakker et al., 2016). The coeval trends in magnetic domain state (ARM_{300}, χARM/IRM), C. *wuellerstorfi* $\delta^{13}C$ negative excursions, and TOC around the end of the penultimate and last glacial cycles (i.e., during MIS 6 and 2), as well as during MIS 4 (Figures 8c–8e) support an association between our magnetic record and changes in the NADW ventilation. Hence, we hypothesize a decrease in the biogenic magnetite production during periods of reduced ventilation.

Notably, between 175 and 145 ka BP, the ARM_{300} intensity and χARM/IRM in our core exhibit values similar to those recorded during MIS 3 and $\delta^{13}C$ shows a positive excursion (Figures 8c–8e). Santos et al (2017) noticed higher variability in $\delta^{13}C$ from early- to mid-MIS 6 in comparison to MIS 3 (Figure 8c). The same study, using Mg/Ca analysis in *G. ruber* shells for core GL-1090, recorded high sea surface temperature variability in the same period (during early-MIS 6). The positive values observed in magnetic grain size parameters and $\delta^{13}C$ during early-MIS 6 may suggests that, exceptionally during this glaciation, biogenic magnetite formation increased in response to ventilation change, which during this period resembles its interglaciation mode, with decreased NADW residence time.

6. Conclusions

In core GL-1090 from the subtropical western South Atlantic mid-depth, magnetic concentration-dependent parameters and major element ratios dominantly reflect glacio-eustatic-modulated changes in the delivery of terrigenous detrital particles. In contrast, changes in magnetic grain-size, likely driven by the concentration of biogenic magnetite, may reflect variations in oceanographic environment during the last ~184 ka. Changes in ln(Al/Si) and Fe/κ indicate that, during periods of low sea-level, sedimentation at this location was dominated by coarser (silt and clay) detrital input from the Plata River, and more Fe was bound to ferromagnetic terrigenous magnetic minerals. Coeval changes in ln(Al/Ti) and ln(K/Ti) support this sediment source interpretation. Conversely, during periods of high sea level, transgressive drowning of the Plata River estuary diminished the northward transport of Plata River sediments by the BCC. During these periods, a mixture between Plata and Paraíba do Sul rives takes place. Decoupled from changes in the terrigenous sources, glacial/interglacial changes in the magneto-granulometric parameters, χARM/IRM and Mrs/Ms together with the SD magnetite concentration parameter ARM_{300}, may reflect variations in the post-depositional formation of biogenic magnetite. The continuous presence of SD magnetite throughout the core suggests that bottom water conditions were favorable both for bacterial magnetite formation and the preservation of magnetofossils. However, coeval declines in SD magnetite concentrations and negative $\delta^{13}C$ values during glacial stages suggest that the reduced ventilation of NADW (or its glacial counterpart) hampered the production of MTB-formed magnetite. In this interpretation, during cold marine isotopic stages, magnetofossil concentrations are lower, directly co-varying with epibenthic foraminifera $\delta^{13}C$ and TOC. Independent, quantitative examination of sediment magnetic extracts would be required in order to test this hypothesis.

Acknowledgments
We thank Stefanie Brachfeld (reviewer), two anonymous reviewers and the anonymous associate editor for constructive comments. This work was supported by CAPES (grants 88882.151090/2017-0, 88881.196484/2018-01 and 88887.177256/2018-00). Cristiano Mazur Chiessi acknowledges financial support from FAPESP (grant 2018/15123-4), CAPES (grants 564/2015 and 88881.313535/2019-01), CNPq (grants 302607/2016-1 and 422255/2016-5) and the Alexander von Humboldt Foundation. M.C. Campos acknowledges the financial support from FAPESP (grant 2016/10242-0). A.L.S. Albuquerque is a senior CNPq researcher (grants 302521-2017-8 and 429767/2018-8), and acknowledges the financial support from CAPES (Finance Code 001, PRINT 88881.310302-2018/01). Sophie C. Roud acknowledges financial support from the Deutsche Forschungsgemeinschaft (grant GI712-16/1). Bruna B. Dias appreciates financial support from CAPES/FAPERJ (grant 202.134/2015). Grasiane L. Mathias acknowledges Prof. Andy Biggin from School of Environmental Sciences, University of Liverpool, UK, and Chuang Xuan and Jin Yuxi from National Oceanography Center (NOC), Southampton, UK, for providing laboratory facilities and friendly receiving me. Janna Just from MARUM, Center for Marine Environmental Sciences, University of Bremen, Germany is thanked for kindly calibrating the EDP-XRF data. This study has benefited from detailed reviews by Prof. Wilbor Poletti, UFVJM, Brazil.

Data Availability Statement

Germany is thanked for kindly calibrating the EDP-XRF data. New data presented herein are archived in Pangaea (https://doi.pangaea.de/10.1594/PANGAEA.922302).

References

Abrajevitch, A., & Kodama, K. (2011). Diagenetic sensitivity of paleoenvironmental proxies: A rock magnetic study of Australian continental margin sediments. *Geochemistry, Geophysics, Geosystems*, *12*. https://doi.org/10.1029/2010GC003481

Amante, C., & Eakins, B. W. (2009). *ETOPO1 1 arc-minute global relief model: Procedures, data sources and analysis* (pp. 1–19). National Geophysical Data Center, NOAA, NOAA Technical Memorandum NESDIS NGDC-24.

Bazylinski, D. A. (1999). Synthesis of the bacterial magnetosome: the making of a magnetic personality. *International Microbiology*, *2*, 71–80.

Bazylinski, D. A., Frankel, R. B., Heywood, B. R., Mann, S., King, J. W., Donaghay, P. L., Hanson, A. K. (1995). Controlled Biomineralization of Magnetite (Fe (inf3) O (inf4)) and Greigite (Fe (inf3) S (inf4)) in a Magnetotactic Bacterium. *Applied and Environmental Microbiology*, *61*, 3232–3239.

Berger, A., & Loutre, M. F. (1991). Insolation values for the climate of the last 10 million years. *Quaternary Science Reviews*, *10*, 297–317.

Blakemore, R., Short, K., Bazylinski, D., Rosenblatt, C., & Frankel, R. B. (1985). Microaerobic conditions are required for magnetite formation within Aquaspirillum magnetotacticum. *Geomicrobiology Journal*, *4*, 53–71.

Bloemendal, J., King, J. W., Hall, F. R., & Doh, S.-J. (1992). Rock magnetism of Late Neogene and Pleistocene deep-sea sediments: Relationship of sediment source, diagenetic processes, and sediment lithology. *Journal of Geophysical Research*, *97*, 4361–4375.

Boebel, O., Davis, R. E., Ollitrault, M., Peterson, R. G., Richardson, P. L., Schmid, C., & Zenk, W. (1999). The intermediate depth circulation of the western South Atlantic. *Geophysical Research Letters*, *26*, 3329–3332.

Bohm, E., Lippold, J., Gutjahr, M., Frank, M., Blaser, P., Antz, B., et al. (2015). Strong and deep Atlantic meridional overturning circulation during the last glacial cycle. *Nature*, *517*, 73–76. https://doi.org/10.1038/nature14059

Campos, M. C., Chiessi, C. M., Venancio, I. M., Pinho, T. M. L., Crivellari, S., Kuhnert, H., et al. (2020). Constraining millennial-scale changes in northern component water ventilation in the western tropical South Atlantic. *Paleoceanography and Paleoclimatology*, e2020PA003876. https://doi.org/10.1029/2020PA003876

Canfield, D. E. (1989). Reactive iron in marine sediments. *Geochimica et Cosmochimica Acta*, *53*, 619–632.

Canfield, D. E., & Thamdrup, B. (2009). Toward a consistent classification scheme for geochemical environments, or, why we wish the term 'suboxic' would go away. *Geobiology*, *7*, 385–392. https://doi.org/10.1111/j.1472-4669.2009.00214.x

Carvalho, L. M. V., Jones, C., & Liebmann, B. (2004). The South Atlantic convergence zone: Intensity, form, persistence, and relationships with intraseasonal to interannual activity and extreme rainfall. *Journal of Climate*, *17*, 88–108. https://doi.org/10.1175/1520-0442(2004)017<0088:TSACZI>2.0.CO;2

Chang, L., Bolton, C. T., Dekkers, M. J., Hayashida, A., Heslop, D., Krijgsman, W., et al. (2016a). Asian monsoon modulation of nonsteady state diagenesis in hemipelagic marine sediments offshore of Japan. *Geochemistry, Geophysics, Geosystems*, *17*, 4383–4398. https://doi.org/10.1002/2016GC006344

Chang, L., Roberts, A. P., Heslop, D., Hayashida, A., Li, J., Zhao, X., et al. (2016b). Widespread occurrence of silicate-hosted magnetic mineral inclusions in marine sediments and their contribution to paleomagnetic recording. *Journal of Geophysical Research: Solid Earth*, *121*, 8415–8431. https://doi.org/10.1002/2016JB013109

Chang, L., Roberts, A. P., Winklhofer, M., Heslop, D., Dekkers, M. J., Krijgsman, W., et al. (2014a). Magnetic detection and characterization of biogenic magnetic minerals: A comparison of ferromagnetic resonance and first-order reversal curve diagrams. *Journal of Geophysical Research: Solid Earth*, *119*, 6136–6158. https://doi.org/10.1002/2014JB011213

Chang, L., Vasiliev, I., Baak, C. V., Krijgsman, W., Dekkers, M. J., Roberts, A. P., et al. (2014b). Identification and environmental interpretation of diagenetic and biogenic greigite in sediments: A lesson from the Messinian Black Sea. *Geochemistry, Geophysics, Geosystems*, *15*, 3612–3627.

Chen, A. P., Berounsky, V. M., Chan, M. K., Blackford, M. G., Cady, C.,Moskowitz, B. M., et al. (2014). Magnetic properties of uncultivated magnetotactic bacteria and their contribution to a stratified estuary iron cycle. *Nature Communications*, *5*, 4797. https://doi.org/10.1038/ncomms5797

Chiessi, C. M., Mulitza, S., Pätzold, J., & Wefer, G. (2010). How different proxies record precipitation variability over southeastern South America. *IOP Conference Series: Earth and Environmental Science*, *9*, 1–6. https://doi.org/10.1088/1755-1315/9/1/012007

Commission for the Geological Map of the World, (CGMW). *Maps for understanding the Earth*. CGMW. Retrieved from https://ccgm.org/

Cruz, F. W., Burns, S. J., Karmann, I., Sharp, W. D., & Vuille, M. (2006). Reconstruction of regional atmospheric circulation features during the late Pleistocene in subtropical Brazil from oxygen isotope composition of speleothems. *Earth and Planetary Science Letters*, *248*, 495–507. https://doi.org/10.1016/j.epsl.2006.06.019

Cruz, F. W., Burns, S. J., Karmann, I., Sharp, W. D., Vuille, M., Cardoso, A. O., et al. (2005). Insolation-driven changes in atmospheric circulation over the past 116,000 years in subtropical Brazil. *Nature*, *434*, 63–65. https://doi.org/10.1038/nature03365

Day, R., Fuller, M., & Schmidt, V. A. (1977). Hysteresis properties of titanomagnetites: Grain size and compositional dependence. *Physics of the Earth and Planetary Interiors*, *13*, 260–267.

de Boer, B., van de Wal, R. S. W., Lourens, L. J., Bintanja, R., & Reerink, T. J. (2012). A continuous simulation of global ice volume over the past 1 million years with 3-D ice-sheet models. *Climate Dynamics*, *41*, 1365–1384. https://doi.org/10.1007/s00382-012-1562-2

Depetris, P. J., Probst, J.-L., Pasquini, A. I., & Gaiero, D. M. (2003). The geochemical characteristics of the Paraná River suspended sediment load: An initial assessment. *Hydrological Processes*, *17*(7), 1267–1277. https://doi.org/10.1002/hyp.1283

Du, H. J., Chen, Y. R., Zhang, R., Pan, H. M., Zhang, W. Y., Zhou, K., et al. (2015). Temporal distributions and environmental adaptations of two types of multicellular magnetotactic prokaryote in the sediments of Lake Yuehu, China. *Environmental Microbiology Reports*, *7*, 538–546. https://doi.org/10.1111/1758-2229.12284

Dunlop, D. J. (1981). The rock magnetism of fine particles. *Physics of the Earth and Planetary Interiors*, *26*, 1–26.

Dunlop, D. J. (2002). Theory and application of the Day plot (Mrs/Ms versus Hcr/Hc) 1. Theoretical curves and tests using titanomagnetite data. *Journal of Geophysical Research*, *107*(B3). https://doi.org/10.1029/2001JB000486

Dunlop, D. J., & Özdemir, Ö. (1997). *Rock magnetism, fundamentals and frontiers* (p. 573). Cambridge Studies in Magnetism.

Egli, R. (2004). Characterization of individual rock magnetic components by analysis of remanence curves, 1. Unmixing natural sediments. *Studia Geophysica et Geodaetica*, *48*, 391–446. https://doi.org/10.1023/B:SGEG.0000020839.45304.6d

Egli, R. (2013). VARIFORC: An optimized protocol for calculating non-regular first-order reversal curve (FORC) diagrams. *Global and Planetary Change*, *110*, 302–320. https://doi.org/10.1016/j.gloplacha.2013.08.003

Egli, R., Chen, A. P., Winklhofer, M., Kodama, K. P., & Horng, C.-S. (2010). Detection of noninteracting single domain particles using first-order reversal curve diagrams. *Geochemistry, Geophysics, Geosystems*, *11*(1), 1–22. https://doi.org/10.1029/2009GC002916

Evans, M. E., & Heller, F. (2003). *Environmental Magnetism Principles and Applications of Enviromagnetics*. International Geophysics Series (86, p. 304). Academic Press.

Faivre, D., & Schüler, D. (2008). Magnetotactic bacteria and magnetosomes. *Chemical Reviews*, *108*, 4875–4898. https://doi.org/10.1021/cr078258w

Figueiredo, T., Santos, T. P., Costa, K. B., Toledo, F., Albuquerqu, A. L. S., Smoak, J. M., et al. (2020). Effect of deep Southwestern Subtropical Atlantic Ocean circulation on the biogeochemistry of mercury during the last two glacial/interglacial cycles. *Quaternary Science Reviews*, *239*. https://doi.org/10.1016/j.quascirev.2020.106368

Funk, J. A., Von Dobeneck, T., & Reitz, A. (2004). Integrated rock magnetic and geochemical quantification of redoxomorphic iron mineral diagenesis in Late Quaternary sediments from the equatorial Atlantic. In G. Wefer, S. Mulitza, & V. Ratmeyer, Eds., *The South Atlantic in the Late Quaternary: Reconstruction of material budgets and current systems* (pp. 237–260). Springer.

Gaiero, D. M., Probst, J. L., Depetris, P. J., Bidart, S. M., & Leleyter, L. (2003). Iron and other transition metals in Patagonian riverborne and windborne materials: geochemical control and transport to the southern South Atlantic Ocean. *Geochimica et Cosmochimica Acta*, *67*(19), 3603–3623. https://doi.org/10.1016/S0016-7037(03)00211-4

Garreaud, R. D., Vuille, M., Compagnucci, R., & Marengo, J. (2009). Present-day South American climate. *Palaeogeography, Palaeoclimatology, Palaeoecology*, *281*, 180–195. https://doi.org/10.1016/j.palaeo.2007.10.032

Gómes Tapias, J., Schobbenhaus, C., & Montes Ramírez, N. E. (2019). *Geological map of south America*. https://doi.org/10.32685/10.143.2019.929

Govin, A., Chiessi, C. M., Zabel, M., Sawakuchi, A. O., Heslop, D., Hörner, T., et al. (2014). Terrigenous input off northern South America driven by changes in Amazonian climate and the North Brazil Current retroflection during the last 250 ka. *Climate of the Past*, *10*, 843–862. https://doi.org/10.5194/cp-10-843-2014

Govin, A., Holzwarth, U., Heslop, D., Keeling, L. F., Zabel, M., Mulitza, S., et al. (2012). Distribution of major elements in Atlantic surface sediments (36°N-49°S): Imprint of terrigenous input and continental weathering. *Geochemistry, Geophysics, Geosystems*, *13*, 1–23. https://doi.org/10.1029/2011GC003785

Grant, K. M., Rohling, E. J., Bar-Matthews, M., Ayalon, A., Medina-Elizalde, M., Bronk Ramsey, C., et al. (2012). Rapid coupling between ice volume and polar temperature over the past 150,000 years. *Nature*, *491*, 744–747. https://doi.org/10.1038/nature11593

Gyllencreutz, R., Mahiques, M. M., Alves, D. V. P., & Wainer, I. K. C. (2010). Mid- to late Holocene paleoceanographic changes on the southeastern Brazilian shelf based on grain size records. *The Holocene*, *20*, 863–875. https://doi.org/10.1177/0959683610365936

Hanzlik, M., Winklhofer, M., & Petersen, N. (1996). Spatial arrangement of chains of magnetosomes in magnetotactic bacteria. *Earth and Planetary Science Letters*, *145*, 125–134.

Hartstra, R. L. (1982). A comparative study of the ARM and Isr os some natural magnetites of MD and PSD grain size. *Geophys. Journal RAS*, *71*, 497–518.

He, K., Roud, S. C., Gilder, S. A., Egli, R., Mayr, C., & Petersen, N. (2018). Seasonal variability of magnetotactic bacteria in a freshwater pond. *Geophysical Research Letters*, *45*, 2294–2302. https://doi.org/10.1002/2018GL077213

Hesse, P. (1994). Evidence for bacterial palaeoecological origin of mineral magnetic cycles in oxic and sub-oxic Tasman Sea sediments. *Marine Geology*, *117*, 1–17.

Hoogakker, B. A. A., Thornalley, D. J. R., & Barker, S. (2016). Millennial changes in North Atlantic oxygen concentrations. *Biogeosciences*, *13*, 211–221. https://doi.org/10.5194/bg-13-211-2016

Hounslow, M. W., & Maher, B. A. (1999). Source of the climate signal recorded by magnetic susceptibility variations in Indian Ocean sediments. *Journal of Geophysical Research*, *104*, 5047–5061.

Howe, J. N. W., Piotrowski, A. M., Noble, T. L., Mulitza, S., Chiessi, C. M., & Bayon, G., et al. (2016). North Atlantic deep water production during the Last Glacial Maximum. *Nature Communications*, *7*, 1–8. https://doi.org/10.1038/ncomms11765

Itambi, A. C., von Dobeneck, T., Mulitza, S., Bickert, T., & Heslop, D. (2009). Millennial-scale northwest African droughts related to Heinrich events and Dansgaard-Oeschger cycles: Evidence in marine sediments from offshore Senegal. *Paleoceanography*, *24*. https://doi.org/10.1029/2007PA001570

Just, J., Dekkers, M. J., von Dobeneck, T., van Hoesel, A., & Bickert, T. (2012a). Signatures and significance of aeolian, fluvial, bacterial and diagenetic magnetic mineral fractions in Late Quaternary marine sediments off Gambia, NW Africa. *Geochemistry, Geophysics, Geosystems*, *13*. https://doi.org/10.1029/2012GC004146

Just, J., Heslop, D., Tilo, D., Bickert, T., Mark, J. D., Thomas, F., et al. (2012b). Multiproxy characterization and budgeting of terrigenous end-members at the NW African continental margin. *Geochemistry, Geophysics, Geosystems*, *13*. https://doi.org/10.1029/2012GC004148

Karlin, R., Lyle, M., & Ross Heath, G. (1987). Authigenic magnetite formation in suboxic marine sediments. *Letters to Nature*, *326*, 490–493.

Kirschvink, J. L., & Chang, S.-B. R. (1984). Ultrafine-grained magnetite in deep-sea sediments: Possible bacterial magnetofossils. *Geology*, *12*, 559–562.

Kopp, R. E., & Kirschvink, J. L. (2008). The identification and biogeochemical interpretation of fossil magnetotactic bacteria. *Earth-Science Reviews*, *86*, 42–61. https://doi.org/10.1016/j.earscirev.2007.08.001

Korff, L., Dobeneck, T. V., Frederichs, T., Kasten, S., Kuhn, G., Gersonde, R., Diekmann, B. (2016). Cyclic magnetite dissolution in Pleistocene sediments of the abyssal northwest Pacific Ocean: Evidence for glacial oxygen depletion and carbon trapping. *Paleoceanography and Paleoclimatology*, *31*, 600–624. https://doi.org/10.1002/2015PA002882

Lippert, P. C. (2008). Big discovery for biogenic magnetite. *Proceedings of the National Academy of Sciences of the United States of America*, *105*, 17595–17596. https://doi.org/10.1073/pnas.0809839105

Lisiecki, L. E., & Raymo, M. E. (2005). A Pliocene-Pleistocene stack of 57 globally distributed benthic δ18O records. *Paleoceanography*, *20*. https://doi.org/10.1029/2004PA001071

Liu, Q., Andrew, P. R., Juan, C. L., Subir, K. B., Yohan, G., Lisa, T., & Frank, O. (2012). Environmental magnetism: Principles and applications. *Reviews of Geophysics*, *50*. https://doi.org/10.1029/2012RG000393

Lovley, D. R., Stolz, J. F., Gordon, L., Nord, J., & Phillips, E. J. P. (1987). Anaerobic production of magnetite by a dissimilatory iron-reducing microorganism. *Nature*, *330*, 252–254.

Lund, D. C., Tessin, A. C., Hoffman, J. L., & Schmittner, A. (2015). Southwest Atlantic water mass evolution during the last deglaciation. *Paleoceanography*, *30*, 477–494. https://doi.org/10.1002/2014PA002657

Mackensen, A., Hubberten, H.-W., Bickert, T., Fischer, G., & Fütterer, D. K. (1993). The δ13C in benthic foraminiferal tests of Fontbotia wuellerstorfi (Schwager) Relative to the δ13C of dissolved inorganic carbon in Southern Ocean Deep Water: Implications for glacial ocean circulation models. *Paleoceanography*, *8*, 587–610.

Mackensen, A., & Schmiedl, G. (2019). Stable carbon isotopes in paleoceanography: Atmosphere, oceans, and sediments. *Earth-Science Reviews*, *197*, 102893. https://doi.org/10.1016/j.earscirev.2019.102893

Maher, B. A. (1988). Magnetic properties of some synthetic sub-micron magnetites. *Geophysical Journal International*, *94*, 83–96.

Maher, B. A. (1998). Magnetic properties of modern soils and Quaternary loessic paleosols: paleoclimatic implications. *Palaeogeography, Palaeoclimatology, Palaeoecology*, *137*, 25–54.

Maher, B. A., & Hounslow, M. W. (1999). The significance of magnetotactic bacteria for the palaeomagnetic and rock magnetic record of Quaternary sediments and soils. In D. H. Tarling, & P. Turner, Eds., *Palaeomagnetism and diagenesis in sediments geological society* (pp. 43–46). Special Publications.

Maher, B. A., Karloukovski, V. V., & Mutch, T. J. (2004). High-field remanence properties of synthetic and natural submicrometre haematites and goethites: significance for environmental contexts. *Earth and Planetary Science Letters*, *226*, 491–505. https://doi.org/10.1016/j.epsl.2004.05.042

Maher, B. A., Prospero, J. M., Mackie, D., Gaiero, D., Hesse, P .P., Balkanski, Y. (2010). Global connections between aeolian dust, climate and ocean biogeochemistry at the present day and at the last glacial maximum. *Earth-Science Reviews*, *99*, 61–97. https://doi.org/10.1016/j.earscirev.2009.12.001

Maher, B. A., & Thompson, R. (1999). *Quaternary climates, environments and magnetism* (p. 390). Cambridge University Press.

Mahiques, M. M., Tassinari, C. C. S., Marcolini, S., Violante, R. A., Figueira, R. C. L., Silveira, I. C. A., et al. (2008). Nd and Pb isotope signatures on the Southeastern South American upper margin: Implications for sediment transport and source rocks. *Marine Geology*, *250*, 51–63. https://doi.org/10.1016/j.margeo.2007.11.007

Marengo, J. A., Liebmann, B., Grimm, A. M., Misra, V., Silva Dias, P. L., Cavalcanti, I. F. A., et al. (2012). Recent developments on the South American monsoon system. *International Journal of Climatology*, *32*, 1–21. https://doi.org/10.1002/joc.2254

Mathias, G. L., Nagai, R. H., Trindade, R. I. F., & de Mahiques, M. M. (2014). Magnetic fingerprint of the late Holocene inception of the Río de la Plata plume onto the southeast Brazilian shelf. *Palaeogeography, Palaeoclimatology, Palaeoecology*, *415*, 183–196. https://doi.org/10.1016/j.palaeo.2014.03.034

Matsuda, T., Endo, J., Osakabe, N., Tonomura, A., & Arii, T. (1983). Morphology and structure of biogenic magnetite particles. *Nature*, *302*, 411–412.

Mulitza, S., Prange, M., Stuut, J. B., Zabel, M., Dobeneck, T. V., Itambi, A. C., et al. (2008). Sahel megadroughts triggered by glacial slowdowns of Atlantic meridional overturning. *Paleoceanography*, *23*(4). https://doi.org/10.1029/2008PA001637

Peters, C., & Dekkers, M. J. (2003). Selected room temperature magnetic parameters as a function of mineralogy, concentration and grain size. *Physics and Chemistry of the Earth*, *28*(16), 659–667. https://doi.org/10.1016/S1474-7065(03)00120-7

Petersen, N., von Dobeneck, T., & Vali, H. (1986). Fossil bacterial magnetite in deep-sea sediments from the South Atlantic Ocean. *Nature*, *320*, 611–615.

Peterson, R. G., & Stramma, L. (1991). Upper-level circulation in the South Atlantic Ocean. *Progress in Oceanography*, *26*, 1–73.

Petschick, R., Kuhn, G., & Gingele, F. (1996). Clay mineral distribution in surface sediments of the South Atlantic: sources, transport, and relation to oceanography. *Marine Geology*, *130*, 203–229.

Piola, A. R., Campos, E. J. D., Möller, O. O., Charo, M., & Martinez, C. (2000). Subtropical Shelf Front off eastern South America. *Journal of Geophysical Research*, *105*, 6565.

Piola, A. R., Matano, R. P., Palma, E. D., Möller, O., Jr, & Campos, E. J. D. (2005). The influence of the Plata River discharge on the western South Atlantic shelf. *Geophysical Research Letters*, *32*. https://doi.org/10.1029/2004GL021638

Portilho-Ramos, R. C., Chiessi, C. M., Zhang, Y., Mulitza, S., Kucera, M., Siccha, M., et al. (2017). Coupling of equatorial Atlantic surface stratification to glacial shifts in the tropical rainbelt. *Scientific Reports*, *7*, 1561. https://doi.org/10.1038/s41598-017-01629-z

Portilho-Ramos, R. D. C., Pinho, T. M. L., Chiessi, C. M., & Barbosa, C. F. (2019). Understanding the mechanisms behind high glacial productivity in the southern Brazilian margin. *Climate of the Past*, *15*, 943–955. https://doi.org/10.5194/cp-15-943-2019

Prospero, J. M., Ginoux, P., Torres, O., Nicholson, S. E., & Gill, T. E. (2002). Environmental characterization of global sources of atmospheric soil dust identified with the Nimbus 7 total ozone mapping spectometer (TOMS) absorbing aerosol product. *Reviews of Geophysics*, *40*(1), 1002. https://doi.org/10.1029/2000RG000095

Razik, S., Chiessi, C. M., Romero, O. E., & von Dobeneck, T. (2013). Interaction of the South American Monsoon System and the Southern Westerly Wind Belt during the last 14kyr. *Palaeogeography, Palaeoclimatology, Palaeoecology*, *374*, 28–40. https://doi.org/10.1016/j.palaeo.2012.12.022

Razik, S., Govin, A., Chiessi, C. M., & von Dobeneck, T. (2015). Depositional provinces, dispersal, and origin of terrigenous sediments along the SE South American continental margin. *Marine Geology*, *363*, 261–272. https://doi.org/10.1016/j.margeo.2015.03.001

Reinholdsson, M., Snowball, I., Zillén, L., Lenz, C., & Conley, D. J. (2013). Magnetic enhancement of Baltic Sea sapropels by greigite magnetofossils. *Earth and Planetary Science Letters*, *366*, 137–150. https://doi.org/10.1016/j.epsl.2013.01.029

Reitz, A., Hensen, C., Kasten, S., Funk, J. A., & de Lange, G. J. (2004). A combined geochemical and rock-magnetic investigation of a redox horizon at the last glacial/interglacial transition. *Physics and Chemistry of the Earth, Parts A/B/C*, *29*, 921–931. https://doi.org/10.1016/j.pce.2004.03.013

Roberts, A. P. (2006). High-resolution magnetic analysis of sediment cores: Strengths, limitations and strategies for maximizing the value of long-core magnetic data. *Physics of the Earth and Planetary Interiors*, *156*, 162–178. https://doi.org/10.1016/j.pepi.2005.03.021

Roberts, A. P., Chang, L., Heslop, D., Florindo, F., & Larrasoaña, J. C. (2012). Searching for single domain magnetite in the "pseudo-single-domain" sedimentary haystack: Implications of biogenic magnetite preservation for sediment magnetism and relative paleointensity determinations. *Journal of Geophysical Research*, *117*. https://doi.org/10.1029/2012JB009412

Roberts, A. P., Chang, L., Rowan, C. J., Horng, C.-S., & Florindo, F. (2011a). Magnetic properties of sedimentary greigite (Fe3S4): An update. *Reviews of Geophysics*, *49*. https://doi.org/10.1029/2010RG000336

Roberts, A. P., Florindo, F., Chang, L., Heslop, D., Jovane, L., Larrasoaña, J. C. (2013). Magnetic properties of pelagic marine carbonates. *Earth-Science Reviews*, *127*, 111–139. https://doi.org/10.1016/j.earscirev.2013.09.009

Roberts, A. P., Florindo, F., Villa, G., Chang, L., Jovane, L., Bohaty, S. M., et al. (2011b). Magnetotactic bacterial abundance in pelagic marine environments is limited by organic carbon flux and availability of dissolved iron. *Earth and Planetary Science Letters*, *310*(3–4), 441–452. https://doi.org/10.1016/j.epsl.2011.08.011

Roberts, A. P., Liu, Q., Rowan, C. J., Chang, L., Carvallo, C., Torrent, J., Horng, C. S. (2006). Characterization of hematite (α-Fe2O3), goethite (α-FeOOH), greigite (Fe3S4), and pyrrhotite (Fe7S8) using first-order reversal curve diagrams. *Journal of Geophysical Research*, *111*. https://doi.org/10.1029/2006JB004715

Roberts, A. P., Pike, C. R., & Verosub, K. L. (2000). First-order reversal curve diagrams: A new tool for characterizing the magnetic properties of natural samples. *Journal of Geophysical Research*, *105*, 28461–28475.

Romero, O., & Hensen, E. (2002). Oceanographic control of biogenic opal and diatoms in surface sediments of the Southwestern Atlantic. *Marine Geology*, *186*(3–4), 263–280. https://doi.org/10.1016/S0025-3227(02)00210-4

Santos, T. P., Lessa, D. O., Venancio, I. M., Chiessi, C. M., Mulitza, S., Kuhnert, H., et al. (2017). Prolonged warming of the Brazil Current precedes deglaciations. *Earth and Planetary Science Letters*, *463*, 1–12. https://doi.org/10.1016/j.epsl.2017.01.014

Savian, J. F., Jovane, L., Frontalini, F., Trindade, R. I. F., Coccioni, R., Bohaty, S. M., et al. (2014). Enhanced primary productivity and magnetotactic bacterial production in response to middle Eocene warming in the Neo-Tethys Ocean. *Palaeogeography, Palaeoclimatology, Palaeoecology*, *414*, 32–45. https://doi.org/10.1016/j.palaeo.2014.08.009

Schlitzer, R. (2019). *Ocean Data View*. Retrieved from https://odv.awi.de

Schmidbauer, E., & Veitch, R. (1980). Anhysteretic remanent magnetization of small multidomain Fe3O4 particles dispersed in various concentrations in a non magnetic matrix. *Journal of Geophysics*, *48*, 148–152.

Schmittner, A., & Lund, D. C. (2015). Early deglacial Atlantic overturning decline and its role in atmospheric CO_2 rise inferred from carbon isotopes ($\delta^{13}C$). *Climate of the Past*, *11*, 135–152. https://doi.org/10.5194/cp-11-135-2015

Sheldon, N. D., & Tabor, N. J. (2009). Quantitative paleoenvironmental and paleoclimatic reconstruction using paleosols. *Earth-Science Reviews*, *95*, 1–52. https://doi.org/10.1016/j.earscirev.2009.03.004

Souza, R. B., & Robinson, I. S. (2004). Lagrangian and satellite observations of the Brazilian Coastal Current. *Continental Shelf Research*, *24*, 241–262. https://doi.org/10.1016/j.csr.2003.10.001

Stolz, J. F., Chang, S.-B. R., & Kirschvink, J. L. (1986). Magnetotactic bacteria and single-domain magnetite in hemipelagic sediments. *Nature*, *321*, 849–851.

Stramma, L., & England, M. (1999). On the water masses and mean circulation of the South Atlantic Ocean. *Journal of Geophysical Research*, *104*, 20863–20883.

Thompson, R., & Oldfield, F. (1986). *Environmental magnetism* (p. 228). Allen & Unwin.

Tsuchiya, M., Talley, L. D., & McCartney, M. S. (1994). Water-mass distributions in the western South Atlantic; A section from South Georgia Island (54S) northward across the equator. *Journal of Marine Research*, *52*, 52–81.

Vali, H., Förster, O., Amarantidis, G., & Petersen, N. (1987). Magnetotactic bacteria and their magnetofossils in sediments. *Earth and Planetary Science Letters*, *86*, 389–400.

Verosub, K. L., & Roberts, A. P. (1995). Environmental magnetism- Past, present, and future. *Journal of Geophysical Research*, *1000*, 2175–2192.

Voigt, I., Cruz, A. P. S., Mulitza, S., Chiessi, C. M., Mackensen, A., Lippold, J., et al. (2017). Variability in mid-depth ventilation of the western Atlantic Ocean during the last deglaciation. *Paleoceanography*, *32*, 948–965. https://doi.org/10.1002/2017PA003095

Weltje, G. J., & Tjallingii, R. (2008). Calibration of XRF core scanners for quantitative geochemical logging of sediment cores: Theory and application. *Earth and Planetary Science Letters*, *274*, 423–438. https://doi.org/10.1016/j.epsl.2008.07.054

Zabel, M., Schneider, R. R., Wagner, T., Adegbie, A. T., Vries, U. D., Kolonic, S. (2001). Late Quaternary climate changes in Central Africa as inferred from terrigenous input to the Niger fan. *Quaternary Research*, *56*(2), 207–217.

Zweng, M. M., Reagan, J. R., Antonov, J. I., Locarnini, R. A., Mishonov, A. V., Boyer, T. P., et al. (2013). *World Ocean Atlas 2013, Volume 2: Salinity*. (S. Levitus, Ed., A. Mishonov Technical Ed.). NOAA Atlas NESDIS 74, p. 39.